Impact of Atmosphere on Geostationary SAR: Performance Analysis and Optimization

Matteo Monti, *Graduate Student Member, IEEE*, Alessandro Gatti, Martina Lagasio, and Andrea Monti Guarnieri, *Senior Member, IEEE*

***Abstract*—Geosynchronous synthetic aperture radar (GEO-SAR) offers a unique capability for wide-area monitoring with persistent observation, leveraging long integration times to compensate for severe path losses at large sensor–target distances. However, spatial and temporal variations in both the troposphere and ionosphere during these long integrations hinder effective azimuth focusing. This article addresses a geosynchronous synthetic aperture radar (SAR) system whose orbit complies with International Telecommunication Union (ITU) regulations for geostationary platforms. Specifically, it investigates optimizing the satellite orbit under constraints imposed by available orbital slots and regulatory requirements. The upper limit on the velocity is determined by additive noise sources (thermal noise, radio frequency interference, and so on), while the lower limit is constrained by the phase noise due to the atmospheric turbulence. The article first develops a statistical model describing the joint variability of ionospheric and tropospheric delays. It then provides a statistical characterization of atmospheric turbulence, which is quantitatively evaluated through the analysis of large datasets obtained from meteorological measurements and global navigation satellite system (GNSS)-based observations. The combination of the performance model and the statistical characterization of atmospheric turbulence enables the optimization of both the system and the satellite orbit. Results show that while a ±0.1° ITU station-keeping box allows for mission feasibility, expanding the tolerance to ±0.5°—still within experimental ITU limits—yields significantly better performance.**

***Index Terms*—Atmospheric phase screen (APS), Earth observing system, geostationary synthetic aperture radar (SAR), ionosphere, multiple aperture interferometry, radar imaging, radar interferometry, troposphere.**

I. Introduction

SPACEBORNE synthetic aperture radar (SAR) is a well-established technology for reliably mapping the Earth's surface and retrieving information about its physical properties, such as topography, morphology, roughness, and the dielectric characteristics of the backscattering layer. SAR interferometry further extends these capabilities, providing a powerful tool for detecting and mapping surface displacements over large temporal and spatial scales with precision in the centimeter and even millimeter range [1], [2], [3], [4], [5].

Received 15 January 2026; revised 23 April 2026; accepted 27 May 2026. Date of publication 1 June 2026; date of current version 9 June 2026. This work was supported by the Agenzia Spaziale Italiana (ASI) and Ministero dell'Università e della Ricerca (MUR) under Contract 2024-5-E.0 and Contract I53D24000060005. *(Corresponding author: Matteo Monti.)*

Matteo Monti and Andrea Monti Guarnieri are with the Dipartimento di Elettronica, Informazione e Bioingegneria Politecnico di Milano (POLIMI-DEIB), 20133 Milan, Italy (e-mail: matteo.monti@polimi.it).

Alessandro Gatti was with the Dipartimento di Elettronica, Informazione e Bioingegneria Politecnico di Milano (POLIMI-DEIB), 20133 Milan, Italy. He is now with e-GEOS, 00156 Rome, Italy.

Martina Lagasio is with CIMA Research Foundation, 17100 Savona, Italy.

Digital Object Identifier 10.1109/TGRS.2026.3698504

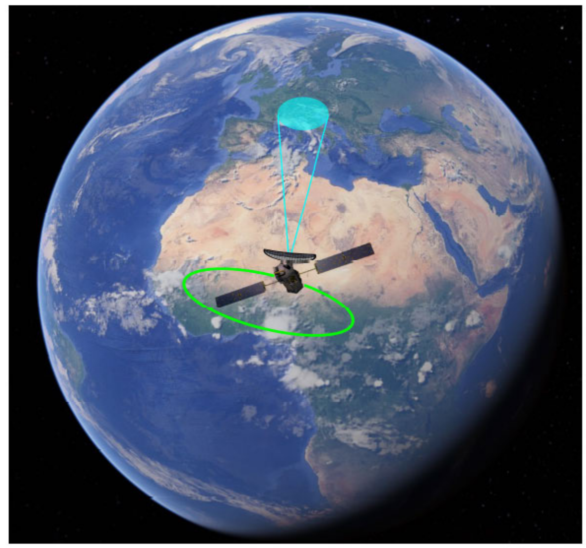

Fig. 1. Representation of an NZI GEO-SAR orbital track. Dimensions are exaggerated [15].

One of the major features of a spaceborne SAR is its day-and-night, all-weather imaging capability, which makes it unique in remote sensing. However, such capability is not fully exploited nowadays, where a daily revisit can be achieved only by dense constellations of low Earth orbit (LEO) SAR, which, however, does provide a limited coverage [6], [7] In recent years, increasing attention has been devoted to geosynchronous SAR missions, which provide a unique capability for persistent observations over very wide swaths, with super-continental access [8]. These systems leverage the long integration time to compensate for the huge path losses due to the distance. Such compensation, however, remains challenging with current technologies due to power and antenna size constraints. Yet, a particular configuration has gained interest thanks to the use of very-long integration time, enabled by a very low velocity, achieved by an orbit with a small eccentricity and/or inclination [9], [10], [11]. An example of the orbit of an International Telecommunication Union (ITU) compliant geostationary satellite with near-zero inclination (NZI) [12] is shown in Fig. 1. The orbit is a small ellipse in the

Earth-centered Earth-fixed (ECEF) frame, which enables the use of integration times—up to several hours—ending in moderate transmission power and medium-sized antennas [11], [13], [14], [15], [16], [17], [18].

The drawback of using a long integration time, however, is the impact of changes in both the target's backscatter and the optical path from the satellite to the target. The target stability has been widely addressed in the literature [19], [20], [21], [22], and it has been shown to be noncritical in systems operating up to the C-band, thanks to the proven long-term stability of the scene [23], [24], [25].

On the other hand, the spatiotemporal variation of the atmospheric delay has been identified in the literature as the primary challenge in such systems [26], [27], [28], [29]. With the term "atmospheric" delay, we refer to the combined contribution of both the tropospheric and the ionospheric propagation.

Indeed, these effects have been widely investigated in the LEO SAR community, together with their estimation and mitigation of their effect on the focused images [2], [21], [30], [31], [32], [33]. However, the temporal variability of these delays was never considered, as it was deemed negligible with respect to the synthetic aperture time, which is on the order of 1 s.

Atmospheric turbulence has been considered in inclined geosynchronous SAR, but only in relation to the ionospheric component, as these were L-band systems, which are loosely affected by the troposphere [34].

In this article, we consider an NZI geosynchronous SAR configuration, assuming a C-band system as a suitable compromise between spatial resolution and scene coherence. The proposed approach can be readily extended to higher frequencies, such as X-band systems. Within this framework, we demonstrate that the turbulent phase fields induced by both the background ionosphere and the troposphere interact over the synthetic aperture time and may hinder proper focusing if they are not accurately estimated and compensated.

To that aim, we adapt and optimize an interferometric-based autofocusing and evaluate the imaging performance as a function of the actual atmospheric turbulence and of the system parameters.

The feasibility of such a mission is driven by the intensity of atmospheric turbulence and the duration of the synthetic aperture time, which, in turn, depend on the orbit's eccentricity. As for the former, a systematic analysis of large tropospheric and ionospheric data is presented here, along with a discussion of the most appropriate statistical models and a quantitative characterization of the associated parameters. As for the orbit, the ITU regulations for geostationary satellites constrain the orbit, in an ECEF frame, to be kept within a maximum longitudinal slot of $\pm 0.1°$ or $\pm 0.5°$ for experimental missions [12], [35]. The corresponding satellite velocity components in the along-track direction with respect to the fixed Earth are shown in Fig. 2 and will be used to check the feasibility and mission performance.

In Section II, we present the qualitative and quantitative modeling of both ionospheric and atmospheric phase screens (APSs), derived from high-resolution Weather Research and Forecasting (WRF) and electronic Space Weather upper atmosphere (eSWua), respectively.

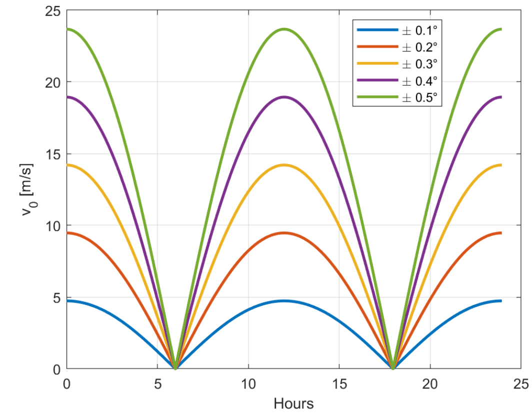

Fig. 2. Along-track velocity component with respect to the fixed Earth of an NZI GEO-SAR for different ITU slots as a function of the time from the perigee.

In Section III, we present a numerical framework for evaluating the impact of joint tropospheric and atmospheric turbulence on long-time integration SAR. The impact has been evaluated in terms of End-to-End (E2E) SAR acquisition and focusing impulse response function (IRF), for the case of an isolated point target, and in terms of coherence for the case of distributed targets. The analysis includes an evaluation of SAR image quality in the presence of additive thermal noise and multiplicative atmospheric phase noise, the most impactful impairments in GEO-SAR.

In Section IV, we use the analysis tool to derive a processing scheme that optimizes image performance and compare theoretical results with simulations. Finally, we assess the mission's feasibility, taking into account compliance with ITU regulations.

II. Model and Values for Atmospheric Turbulence

A. Tropospheric Turbulence

The propagation of electromagnetic waves in the troposphere is affected by a delay related to the refractive index, which depends on temperature, pressure, and humidity [36], [37]. The resultant delay causes the optical path to exceed the geometric one by several meters. However, the largest portion of this delay varies slowly over time and has little or no impact on SAR acquisition, whereas SAR focusing is mostly influenced by the fast temporal and spatial variations of water vapor. The wet delay (WD) is typically on the order of 1 cm (one-way) but may reach 30 cm or more under strong turbulent conditions [2], [38], [39], [40].

To quantify the impact of the turbulent tropospheric field—here referred to as the WD—on SAR images, both the structure function and the variogram have been proposed in the literature [27], [28], [30], [34], [41]. The structure function describes how differences in the refractive index affect propagation; thus, given the statistics of the refractive index, one can derive the delay integrated over the column and then its statistics.

A second approach consists of directly modeling the variogram of the integrated delay, which is the physical quantity affecting SAR observations and focusing [26], [27], [42]. In this article, we adopt this second approach as it is more directly related to SAR acquisition and focusing.

The variogram of the WD follows a power-law behavior, first introduced by Kolmogorov [43] and later confirmed by extensive literature. In GEO-SAR systems, the extended and oblique atmospheric path amplifies these effects, particularly the wet component, which may introduce significant phase noise in interferometric applications. The resulting WD d_T represents the extra path introduced by the reduced propagation velocity with respect to c [44]

$$d_T = \int (v - c)\, dt = \int (n - 1)\, dl = 10^{-6} \int N\, dl \tag{1}$$

where v is the signal propagation velocity, n is the refractive index along the signal path, and $N = 10^6(n-1)$ is the radio refractivity. The WD is nondispersive and varies with time and space; however, unlike the ionospheric delay, it can be assumed to be isotropic. High-resolution numerical weather models can be used for tropospheric delay correction [38], [39], [45], [46]. These corrections have been shown to provide some mitigation for the spatial turbulence in LEO-SAR cases, but they are much less effective for a GEO-SAR, as they do not provide the needed spatiotemporal resolution [26], [27], [34], [42], [47].

The following joint time–space model for the WD variogram was proposed in [41] as a straightforward extension of the Kolmogorov power law, which has been widely validated separately in both the temporal and spatial domains

$$\begin{aligned} 2V_T(\tau, x) &= \mathbb{E}\left[|d_T(t+\tau, \chi + x) - d_T(t, \chi)|^2\right] \\ &= \frac{2\sigma_T^2}{\cos^2\theta}\left[1 - \exp\left(-\sqrt{\left(\frac{\tau}{\tau_T}\right)^2 + \left(\frac{x}{x_T}\right)^2}\right)\right] \end{aligned} \tag{2}$$

where d_T is the WD, σ_T^2 is the tropospheric sill, θ is the incidence angle, τ_T is the tropospheric decorrelation time, x_T is the tropospheric decorrelation length, τ is the along-track time lag, and x is the azimuthal separation.

The variogram in (2) is well-suited for modeling the impact of tropospheric turbulence in long-integration-time SAR. However, its use had been limited due to the lack of quantitative information on turbulence at the required fine temporal and spatial resolutions. In fact, LEO-SAR provides information at a very dense spatial resolution (hundreds of meters) but with a coarse temporal resolution (days), whereas the global navigation satellite system (GNSS) is sparse in the spatial domain but almost continuous in time. Even with meteorological models, there remains a lack of data, particularly at fine sampling in the joint space and time [48].

However, recent advances in meteorological models have enabled the systematic production of maps with fine temporal and spatial resolutions. In this article, we processed a large dataset spanning an entire year, sampled at 1.5 km/h, to verify the model (2) and provide statistics on the model parameters, which enable a quantitative assessment of tropospheric turbulence. The results, discussed in Appendix A, drive the performance assessment and optimization that is the object of this article.

B. Ionospheric Turbulence

The ionosphere is a dispersive plasma layer extending from approximately 50 to 1000 km above Earth, composed of free electrons and ionized particles, with the electron density peaking around 400 km. It is well established that ionospheric propagation effects significantly impact signal properties, causing a phase delay that is more pronounced at lower radar frequencies (e.g., P-band and L-band). This delay is inversely proportional to the carrier frequency and directly related to the total number of electrons encountered along the propagation path, resulting in the case of LEO SAR in image shift, distortion, and resolution degradation [49], [50].

However, for a GEO-SAR, the frozen-time assumption that holds for a LEO-SAR is no longer valid, and the variation of the background ionosphere becomes a major source of image degradation, causing defocusing and delays [33], [51]. So far, the impact of the ionosphere has been limited to the case of geostationary SAR operating in the L-band. The analysis of a geostationary SAR in the C-band is quite different since, on the one hand, the synthetic aperture is much longer due to the lower velocity (orders of magnitude), and on the other hand, the dispersion in the C-band is much lower than for L-band at similar resolution.

The magnitude of the single-pass delay at nadir can be computed by [51]

$$d_I(\lambda) = \frac{K}{c^2} \cdot \lambda^2 \tag{3}$$

expressed in total electron content unit (TECU) (10^{16} e$^-$/m^2), where $K = 40.28$ m^3/s^2, c is the speed of light, and λ is the wavelength.

For the C-band, a variation of 1 TECU gives from (3) a phase shift of 3.1 rad, which would greatly degrade the quality of the focused data. In [33], TEC variations of 2–3 TECU over 1000 s are reported for the few cases considered. Such variations will totally jeopardize GEO-SAR focusing, unless properly compensated and mitigated.

This motivates an extensive analysis of the fluctuation of the ionospheric delay and its associated phase. In Appendix B, we report statistics derived by modeling ionospheric delay variograms in space and time and validating them with over one year of maps of vertical total electron content (VTEC), provided by the Italian National Institute of Geophysics and Volcanology (INGV) [52]

From the results in Appendix B, we can deduce that the impact of ionospheric turbulence on the C-band (and higher frequencies) is essentially in its temporal structure. To get this, let us evaluate the interval in which the ionospheric phase standard deviation changes by less than one radian, which is usually assumed as a limit for proper focusing, according to the depth of focusing criterion [53]. This interval is less than 17 s during the most turbulent period of the year (Spring) according to the statistics in Appendix B for observations at

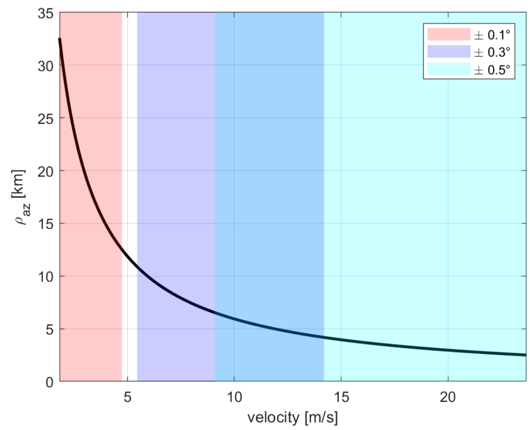

Fig. 3. Azimuth resolution achieved in 17 s at the height of the ionosphere layer for different values of the satellite velocity.

40° N. In such an interval, a synthetic aperture can be formed, giving an azimuth resolution

$$\rho_{az}(R) = \frac{\lambda}{2v_0 \cdot T_s} \cdot R \tag{4}$$

where T_s is the integration time and R is the distance from the satellite. This resolution corresponds to a patch of 2–30 km, measured at the height of the ionospheric screen (R = 37 000–38 000 km), and plotted in Fig. 3 for different values of the velocity. The colored bands represent the allowable SAR acquisition velocities for each ITU slot, i.e., from 1.5 h after the ascending node to perigee.

The worst case resolution is ~30 km, and over this scale, the spatial variation of the ionosphere, as computed in Appendix B, is less than 0.8 rad. This is sufficient for focusing, allowing us to conclude that the ionosphere can be modeled using its temporal variogram

$$2V_I(\tau) = \frac{2\alpha_I}{\cos^2\theta}|\tau| \tag{5}$$

where α_I is the delay rate expressed in mm^2/s. As detailed in Appendix B, this model is based on a statistical analysis of VTEC maps derived from GNSS measurements provided by the eSWua database. The fitting errors, which are on the order of a few percent, are consistent with the Kolmogorov turbulence model for the ionosphere [54].

III. Impact of Atmospheric Turbulence on GEO-SAR Focused Images

The quantitative analysis of tropospheric and ionospheric turbulence presented in Appendices A and B highlights the need to jointly model their impact on geostationary SAR. This joint modeling is essential to derive an effective mitigation approach, evaluate the achievable performance, and ultimately assess the mission's feasibility. This section addresses a gap by providing a unified model that can assess the combined influence of both atmospheric layers on GEO-SAR imaging performance.

A. Acquisition Model

The consolidated approach for mitigating the APS in long-term focusing SAR is the processing of short subapertures [26], [27], [28], [47]. In a short interval, the range compressed data s_{rc} can be modeled as monodimensional, in the slow-time τ

$$s_{rc}(\tau) = w(\tau)\, e^{j\phi_I(\tau)} \int s(x)\, e^{-j\frac{4\pi}{\lambda}\Delta R(\tau,x)} e^{j\phi_T(\tau,x)}\, dx \tag{6}$$

where ΔR is the path delay from a target at azimuth x to the sensor at slow time τ, w is the window superposed to the synthetic aperture, $\phi_T(\tau, x)$, the spatial–temporal tropospheric phase screen and $\phi_I(\tau)$, the temporal ionospheric one.

The mathematical formulation provided by (6) is typically approximated by the Fourier transform, which maps it into the Doppler domain, in the case of a rectilinear track. This would need to estimate the Fourier transform of the variograms and the aperture window, in the discrete case, to which we prefer the exact numeric representation

$$\mathbf{s}_{rc} = (\mathbf{\Phi}_R \odot \mathbf{W} \odot \mathbf{\Phi}_T \odot \mathbf{\Phi}_I)\, \mathbf{s} \tag{7}$$

where $\odot$ represents the Hadamard product and $\boldsymbol{s}_{rc}$ is the $[N_x \times 1]$ column vector of N_x complex samples of the SAR reflectivity along azimuth. In the equation, the matrices $\mathbf{\Phi}_I$ and $\mathbf{\Phi}_T$ of size $[N_\tau \times N_x]$ implement the random ionospheric and tropospheric phase screens, $\mathbf{W}$ is the subaperture window, made by N_x identical columns, and $\mathbf{\Phi}_R$ is the discretization of the first exponential in (6), which accounts for phase due to the travel path distance $\Delta R(\tau_n, x_m) = |P(x_m) - S(\tau_n)|$. Without loss of generality, we may assume atmospheric delay to be null at a specific time origin

$$\mathbf{\Phi}_T(n,m) = \exp\left(j\frac{4\pi}{\lambda}\left(d_T(\tau_n, x_m) - d_T(0,0)\right)\right)$$
$$\mathbf{\Phi}_I(n,m) = \exp\left(j\frac{4\pi}{\lambda}\left(d_I(\tau_n) - d_I(0)\right)\right)$$
$$\forall m \in \{1, \ldots, N_x\} \tag{8}$$

where d_T and d_I have been defined in (1) and (3). The formulation in (8) defines the atmospheric phase relative to a specific time origin, $t = 0$. This approach effectively removes the mean atmospheric delay (the "background" component), which typically varies on much longer scales than the synthetic aperture time. By referencing the phase to the start of the aperture, we focus on the turbulent fluctuations (d_T and d_I). These fluctuations are modeled as zero-mean stochastic processes, as is standard in the Kolmogorov-based turbulence theory.

B. E2E Model

SAR focusing is implemented, as usual, by the matched phase filter, applied to the windowed subaperture, $\boldsymbol{s}_{rc}$ in (7)

$$\hat{\mathbf{s}}_{APS} = \mathbf{\Phi}_R^H (\mathbf{\Phi}_R \odot \mathbf{W} \odot \mathbf{\Phi}_T \odot \mathbf{\Phi}_I)\, \mathbf{s} = \mathbf{H}\,\mathbf{s} \tag{9}$$

where $\mathbf{\Phi}_R^H$ is the Hermitian transposition of the APS-free acquisition phasor. The operator $\mathbf{H}$ provides a compact formulation for the E2E SAR acquisition and focusing in the presence of atmospheric disturbances.

This matrix formulation enables the performance evaluation under various ionospheric, tropospheric, and orbital conditions, as well as for different parameters such as the aperture window. Finally, we utilize the statistics from Section II and Appendices A and B to evaluate the IRF in terms of its mean value, standard deviation, and the decorrelation resulting from the turbulent atmosphere. To account for the random nature of atmospheric phenomena, this evaluation is achieved by deriving theoretical models and validating them through Monte Carlo simulations.

C. Impulse Response Function

To assess the impact of the ionosphere and troposphere on a focused geostationary image without compensating for the APS, the SAR focusing quality is evaluated in terms of the shape of the squared amplitude of the IRF

$$\mathbf{H}_{\text{IRF}} = |\mathbf{H}|^2 = \left[\operatorname{diag}\left(\hat{\mathbf{s}}_{APS} \cdot \hat{\mathbf{s}}_{APS}^{H}\right)\right]. \tag{10}$$

In our case, the IRF in (10) is stochastic due to the randomness of the atmospheric component $\mathbf{\Phi_T} \odot \mathbf{\Phi_I}$ in (9). This is a major departure from a conventional LEO-SAR, where APS is frozen during the short acquisition interval and, thus, acts only as a constant phase shift. The IRF quality needs to be evaluated in terms of the mean value and the variance $\mathbf{H}_{\text{IRF}}$.

The mean value results by combining (10) and (8)

$$\begin{aligned}\mathbb{E}\left[\mathbf{H}_{\text{IRF}}(x_i)\right] = \sum_{k=1}^{N_\tau}\sum_{l=1}^{N_\tau} & \mathbf{\Phi}_R^*(\tau_k, x_i)\, \mathbf{\Phi}_R(\tau_l, x_i) \\ & \cdot \mathbf{\Phi}_R(\tau_k)\, \mathbf{\Phi}_R^*(\tau_l)\, \mathbf{w}(\tau_k)\, \mathbf{w}(\tau_l) \\ & \cdot \mathbb{E}\left[\mathbf{\Phi}_T(\tau_k)\, \mathbf{\Phi}_T^*(\tau_l)\right] \mathbb{E}\left[\mathbf{\Phi}_I(\tau_k)\, \mathbf{\Phi}_I^*(\tau_l)\right].\end{aligned} \tag{11}$$

The mean value can be computed by the double summation and by replacing the two expectations with the value derived from the variograms in (2) and (5)

$$\begin{aligned}\mathbb{E}\left[\mathbf{\Phi}_T(\tau_k)\, \mathbf{\Phi}_T^*(\tau_l)\right] &= \exp\left(-\left(\tfrac{4\pi}{\lambda}\right)^2 \tfrac{\sigma_T^2}{\cos^2\theta}\right. \\ &\quad \left.\cdot\left(1 - \exp\left(-\sqrt{\left(\tfrac{\tau_k - \tau_l}{\tau_T}\right)^2}\right)\right)\right) \\ \mathbb{E}\left[\mathbf{\Phi}_I(\tau_k)\, \mathbf{\Phi}_I^*(\tau_l)\right] &= \exp\left(-\left(\tfrac{4\pi}{\lambda}\right)^2 \tfrac{\alpha_I}{\cos^2\theta}\left|\tau_k - \tau_l\right|\right).\end{aligned} \tag{12}$$

The variance of the IRF can also be derived from (10)

$$\begin{aligned}\operatorname{var}(\mathbf{H}_{\text{IRF}}) &= \mathbb{E}\left[\operatorname{diag}\left(\hat{\mathbf{s}}_{APS}^H \hat{\mathbf{s}}_{APS}\right) \odot \operatorname{diag}\left(\hat{\mathbf{s}}_{APS}^H \hat{\mathbf{s}}_{APS}\right)\right] \\ &\quad - \left|\mathbb{E}\left[\operatorname{diag}\left(\hat{\mathbf{s}}_{APS}^H \hat{\mathbf{s}}_{APS}\right)\right]^2\right|.\end{aligned} \tag{13}$$

We remind that $\hat{\mathbf{s}}_{APS}$ is the focused IRF, distorted by the atmospheric phase—the stochastic component—and back-projected on the ground. For the central limit theorem, we assume the back-projection to be normally distributed, and then, in virtue of the moment theorem for normal processes, we can develop (13)

$$\begin{aligned}\operatorname{var}(\mathbf{H}_{\text{IRF}}) &= 2\mathbb{E}\left[\operatorname{diag}\left(\hat{\mathbf{s}}_{APS}^H \hat{\mathbf{s}}_{APS}\right)\right] \mathbb{E}\left[\operatorname{diag}\left(\hat{\mathbf{s}}_{APS}^H \hat{\mathbf{s}}_{APS}\right)\right] \\ &\quad + \mathbb{E}\left[\operatorname{diag}\left(\hat{\mathbf{s}}_{APS}^H \hat{\mathbf{s}}_{APS}^H\right)\right] \mathbb{E}\left[\operatorname{diag}\left(\hat{\mathbf{s}}_{APS} \hat{\mathbf{s}}_{APS}\right)\right] \\ &\quad - \left|\mathbb{E}\left[\operatorname{diag}\left(\hat{\mathbf{s}}_{APS}^H \hat{\mathbf{s}}_{APS}\right)\right]^2\right| \\ &= \left|\mathbb{E}\left[\operatorname{diag}\left(\hat{\mathbf{s}}_{APS}^H \hat{\mathbf{s}}_{APS}\right)\right]^2\right| \\ &\quad + \mathbb{E}\left[\operatorname{diag}\left(\hat{\mathbf{s}}_{APS}^H \hat{\mathbf{s}}_{APS}^H\right)\right] \mathbb{E}\left[\operatorname{diag}\left(\hat{\mathbf{s}}_{APS} \hat{\mathbf{s}}_{APS}\right)\right] \\ &= \left|\mathbb{E}\left[\operatorname{diag}\left(\hat{\mathbf{s}}_{APS}^H \hat{\mathbf{s}}_{APS}\right)\right]^2\right| = \left(\mathbb{E}\left[\mathbf{H}_{\text{IRF}}\right]\right)^2.\end{aligned} \tag{14}$$

TABLE I
GEO-SAR SYSTEM AND ATMOSPHERIC TURBULENCE PARAMETERS

θ	50°
λ	0.056 m
T_s	3600 s
τ_T	10 h
x_T	10 km
σ_T^2 (normal)	100 mm^2
σ_T^2 (turbulent)	600 mm^2
α_I	0.44 mm^2/s
X_s	10 km

This final formulation, achieved by considering that both tropospheric and ionospheric phasors have zero mean from (8), shows that the variance equals the square of the mean value in (11). This implies that the standard deviation of the IRF is equal to its mean. The assumption of zero mean atmospheric phasors holds when the two-way delay is comparable or larger than the wavelength, that is, from (27)

$$\sigma_s^2 = \left(\frac{4\pi}{\lambda}\right)^2 \frac{\sigma_T^2}{\cos^2\theta} \gg \pi. \tag{15}$$

This is the case for C-band even with normal tropospheric conditions, where $\sigma_T^2 = 100$ mm^2 [2], [41], and then, $\sigma_s^2 \sim 12$. Any residual nonzero mean component introduces an additive phase constant, which superimposes onto the defocusing term primarily induced by zero-mean turbulent fluctuations, potentially leading to undesired phase wrapping.

To validate the expressions for the mean and variance of the IRF, we conducted a Monte Carlo simulation using the system parameters listed in Table I. These parameters refer to a C-band mission pointing at mid-latitudes, with an image time limited to 1 h. As described in previous analyses in [28] and [55], the troposphere can be in normal ($\sigma_T^2 = 100$ mm^2) or turbulent conditions, depending on the sill value. As the ionospheric parameter α_I, described in Appendix B, the value $\alpha_I = 0.44$ mm^2/s has been considered. For the decorrelation time and space of the troposphere, typical literature values of $\tau_T = 10$ h and $x_T = 10$ km have been taken, which have also been confirmed in the statistical analysis of Appendix A [28], [41], [42], [48], [56], [57].

In the simulation, several runs of acquisition and focusing have been carried out by implementing (10), where random APSs were generated as colored Gaussian noise, by using the Von Karman spectrum, as from reference [58], to match the variograms in (2) and (5).

The mean and standard deviations of the resulting IRF have been plotted in Fig. 4, on the top, and compared with the numerical model from (11) and (12). As an intermediate case for the ±0.5° slot GEO orbit, the velocity of the satellite is assumed to be 16 m/s, and the integration time is 1 h. The case of the normal troposphere of the Table I is considered,

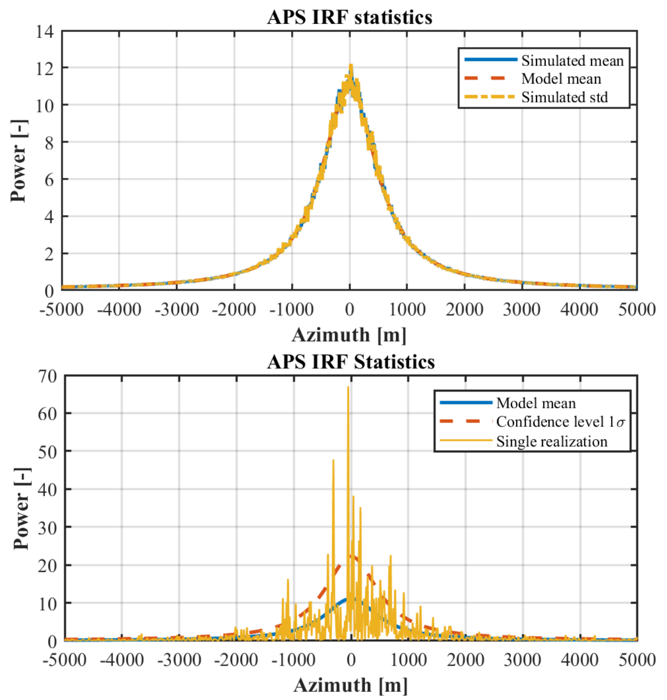

Fig. 4. Expected value and standard deviation of (top) IRF and (bottom) example of a single random IRF. The satellite velocity is 16 m/s, and the integration time is 1 h. The azimuth resolution is 1150 m.

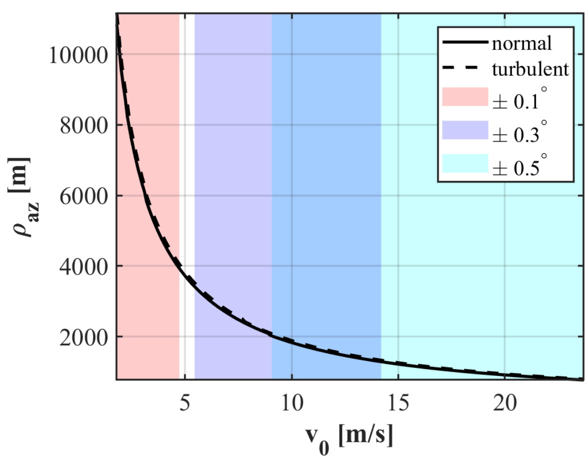

Fig. 5. Azimuth resolution of the IRF in the presence of APS as a function of the satellite velocity by assuming a Hamming window and both normal and turbulent tropospheres.

and the window function is rectangular. The match is good enough to validate the model proposed here. In the same figure, on the bottom, a random realization of the IRF has been plotted to appreciate the impact of the APS. We observe that this realization is reasonably bounded around the mean IRF, with the standard deviation from (14) used as error bars. It can be noted that the impact of the turbulent APS is really a distortion of the IRF, which includes a shift, but is not limited to that. This implies that autofocusing methods based on the estimation of IRF shifts, which are commonly used in LEO SAR, are not effective in this case.

The analysis was conducted using two window functions: rectangular and Hamming. The Hamming window has been introduced to reduce sidelobes, which are too high with a simple rectangular window. In Fig. 5, the azimuth resolution of the IRF in the presence of APS as a function of the satellite velocity is represented. In this case, the Hamming window is considered and applied under both normal and turbulent tropospheric conditions. The dominance of the ionosphere is evident, given that resolution performance remains largely unaffected by the transition from normal to turbulent tropospheric states.

D. Distributed Target

While the quality of the IRF is used to assess E2E performance on point targets, the coherence is the metric widely adopted for distributed targets and, more specifically, the coherence between an APS-free and an APS-affected image

$$\gamma_{APS} = \frac{\mathrm{tr}\left(\mathbb{E}\left[\hat{\mathbf{s}}\,\hat{\mathbf{s}}_{\mathbf{APS}}^{\mathbf{H}}\right]\right)}{\sqrt{\mathrm{tr}\left(\mathbb{E}\left[\hat{\mathbf{s}}\hat{\mathbf{s}}^{\mathbf{H}}\right]\right)\cdot\mathrm{tr}\left(\mathbb{E}\left[\hat{\mathbf{s}}_{\mathbf{APS}}\hat{\mathbf{s}}_{\mathbf{APS}}^{\mathbf{H}}\right]\right)}} \tag{16}$$

where the APS-free image is retrieved as

$$\hat{\mathbf{s}} = \mathbf{\Phi}_R^H\left(\mathbf{\Phi}_R \odot \mathbf{W}\right)\mathbf{s}. \tag{17}$$

Also, for this quality figure, we can provide an ”exact” numerical model by combining (9) and (16)

$$\gamma_{APS} = \frac{\left|\mathrm{tr}\left[\mathbf{H}_{\mathbf{ref}}\left(\mathbf{\Phi}_{\mathbf{eaps}}\mathbf{\Phi}_{\mathbf{R}}\right)\right]\right|}{\sqrt{\mathrm{tr}\left(\mathbf{H}_{\mathbf{ref}}^{\mathbf{H}}\mathbf{H}_{\mathbf{ref}}\right)\cdot\mathrm{tr}\left(\mathbf{H}_{\mathbf{ref}}^{\mathbf{H}}\mathbf{H}_{\mathbf{ref}}\right)}} \tag{18}$$

where

$$\mathbf{H}_{\mathbf{ref}} = \mathbf{\Phi}_{\mathbf{R}}^{\mathbf{H}}\left(\mathbf{\Phi}_R \odot \mathbf{W}\right) \tag{19}$$

and

$$\mathbf{\Phi}_{\mathbf{eaps}} = \mathbf{\Phi}_{\mathbf{R}} \odot \mathbf{W} \odot \mathbb{E}\left[\mathbf{\Phi}_T\right] \odot \mathbb{E}\left[\mathbf{\Phi}_I\right]. \tag{20}$$

The expected values of the two matrices on the right can be derived from the variograms of the troposphere (2) and the ionosphere (5)

$$\begin{aligned}\mathbb{E}\left[\mathbf{\Phi}_T(\tau,x)\right] &= \exp\left(-\left(\tfrac{4\pi}{\lambda}\right)^2\frac{\sigma_T^2}{\cos^2\theta}\right.\\ &\qquad\left.\cdot\left(1-\exp\left(-\sqrt{\left(\tfrac{\tau}{\tau_T}\right)^2+\left(\tfrac{x}{x_T}\right)^2}\right)\right)\right)\\ \mathbb{E}\left[\mathbf{\Phi}_I(\tau)\right] &= \exp\left(-\left(\tfrac{4\pi}{\lambda}\right)^2\frac{\alpha_I}{\cos^2\theta}\,|\tau|\right).\end{aligned} \tag{21}$$

The desired coherence estimate results from numerical evaluation of (18), (19), and (21). It is worth noting in (18) that the denominator simplifies to the square of the same term, implying that the total power of the APS-affected image is identical to that of the APS-free case. This consistency stems from the unit modulus of the atmospheric phasors discussed in Section III, which ensures that the atmosphere acts as a phase-only (or purely dispersive) medium without introducing power attenuation. This numerical model is flexible with respect to variogram models and different window shapes and can be used to optimize the estimation and compensation of APS and then evaluate the mission feasibility.

An approximated, simple expression can be provided by generalizing the one in [28], derived for the sole tropospheric component and assuming rectangular windowing for the subaperture, under the assumption of uniformity within the azimuth resolution cell

$$\hat{\gamma}_{APS} = \frac{1}{\rho_{az} T_s} \int_{-T_s/2}^{T_s/2} \int_{-\rho_{az}/2}^{\rho_{az}/2} \mathbb{E}\left[\mathbf{\Phi_T}(\tau, x)\right] \mathbb{E}\left[\mathbf{\Phi_I}(\tau)\right] \, dx \; d\tau. \tag{22}$$

The expression can be further approximated by decomposing it into the temporal and spatial components, $\hat{\gamma}_\tau$ and $\hat{\gamma}_x$

$$\hat{\gamma}_{APS} = \frac{1}{T_s} \int_{-\frac{T_s}{2}}^{\frac{T_s}{2}} \mathbb{E}\left[\mathbf{\Phi_T}(\tau, 0)\right] \mathbb{E}\left[\mathbf{\Phi_I}(\tau)\right] d\tau \cdot \frac{1}{\rho_{az}} \int_{-\frac{\rho_{az}}{2}}^{\frac{\rho_{az}}{2}} \mathbb{E}\left[\mathbf{\Phi_T}(0, x)\right] \, dx = \hat{\gamma}_\tau \cdot \hat{\gamma}_x. \tag{23}$$

By solving the integrals of (23) separately, $\hat{\gamma}_\tau$ and $\hat{\gamma}_x$ are computed as follows:

$$\begin{aligned}
\hat{\gamma}_\tau &= \frac{1}{T_s} \int_{-T_s/2}^{T_s/2} e^{-\left(\frac{4\pi}{\lambda}\right)^2 \frac{\sigma_T^2}{\cos^2\theta} \frac{|\tau|}{\tau_T}} e^{-\left(\frac{4\pi}{\lambda}\right)^2 \frac{\alpha_I}{\cos^2\theta} |\tau|} \, d\tau \\
&= \frac{2}{T_s} \int_0^{T_s/2} e^{-\xi_0 \tau} \, d\tau \\
&= \frac{2}{T_s \xi_0} \left(1 - \exp\left(-\frac{T_s \xi_0}{2}\right)\right)
\end{aligned} \tag{24}$$

$$\begin{aligned}
\hat{\gamma}_x &= \frac{1}{\rho_{az}} \int_{-\rho_{az}/2}^{\rho_{az}/2} e^{-\left(\frac{4\pi}{\lambda}\right)^2 \frac{\sigma_T^2}{\cos^2\theta} \frac{|x|}{x_T}} \, dx \\
&= \frac{2}{\rho_{az}} \int_0^{\rho_{az}/2} e^{-\frac{\sigma_{0_T}^2}{x_T} x} \, dx \\
&= \frac{2 x_T}{\rho_{az} \sigma_{0_T}^2} \left(1 - \exp\left(-\frac{\rho_{az} \sigma_{0_T}^2}{2 x_T}\right)\right) \\
&= \frac{4 x_T v_0 T_s}{\sigma_{0_T}^2 \lambda R_0} \left(1 - \exp\left(-\frac{\sigma_{0_T}^2 \lambda R_0}{4 x_T v_0 T_s}\right)\right)
\end{aligned} \tag{25}$$

where

$$\begin{aligned}
\xi_0 &= \frac{\sigma_{0_T}^2}{\tau_T} + \alpha_{0_I} \\
\sigma_{0_T}^2 &= \left(\frac{4\pi}{\lambda}\right)^2 \frac{\sigma_T^2}{\cos^2\theta} \\
\alpha_{0_I} &= \left(\frac{4\pi}{\lambda}\right)^2 \frac{\alpha_I}{\cos^2\theta}.
\end{aligned} \tag{26}$$

In this way, from (22), (24), (25), and (26), the coherence given by the total APS is

$$\hat{\gamma}_{APS} = \frac{8 x_T v_0}{\xi_0 \, \sigma_{0_T}^2 \, \lambda \, R_0} \left(1 - \exp\left(-\frac{T_s \xi_0}{2}\right)\right) \cdot \left(1 - \exp\left(-\frac{\sigma_{0_T}^2 \, \lambda \, R_0}{4 x_T v_0 T_s}\right)\right). \tag{27}$$

E. APS Estimation: Optimal Subaperture Time

Based on the performance analysis presented, it becomes clear that a geostationary SAR system cannot produce high-quality, well-focused images unless the ionospheric distortions and atmospheric turbulence are properly estimated and compensated.

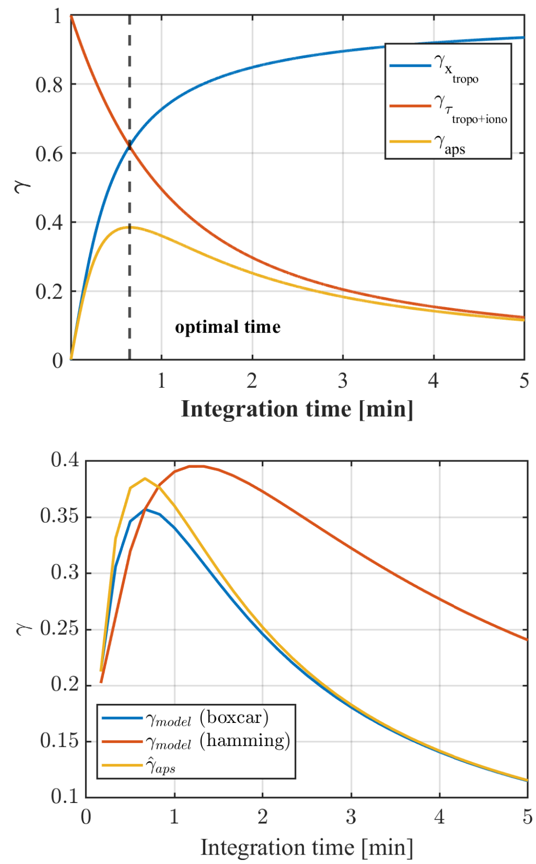

Fig. 6. Coherence between APS-free focused data and APS-affected ones as a function of integration time for $\sigma_T^2 = 100$ mm^2 and $v_0 = 16$ m/s. (Top) Spatial, temporal, and total coherences from the approximate model (27). (Bottom) Comparison of the approximate model (yellow) with the exact numerical boxcar result (blue) and the Hamming-window result (red).

The subapertures approach is the most effective for estimation and compensation [26], [27], [28], [47]. They are based on the idea that, in a short subaperture, turbulence has a negligible impact, allowing the computation of a coarse-resolution focused image. This image is then combined interferometrically with a reference one to retrieve the APS.

The effectiveness of this approach critically depends on the subaperture duration and the quality of the coarsely focused SAR image. As in [28], the optimal subaperture time is derived as the value T_s that balances the temporal decorrelation with the spatial decorrelation [see (24) and (25)]. This can be derived via a proportionality (scaling) argument subject to the time–bandwidth product constraint

$$\begin{aligned}
\xi_0 T_o &= \frac{\sigma_{0_T}^2}{x_T} \rho_{az} \\
T_o &= \sqrt{\frac{\sigma_{0_T}^2 \, \lambda \, R_0}{2 \; v_0 \, x_T \, \xi_0}}.
\end{aligned} \tag{28}$$

Fig. 6 shows the temporal and spatial coherence, as a function of subaperture time, which can be expected in normal tropospheric and ionospheric conditions as defined in

Appendices A and B, and by assuming the parameters used in Table I and a satellite velocity of 16 m/s.

One can observe that the variation in the background ionosphere increases temporal decorrelation and reduces optimal time and coherence. The shortening of T_o is critical since the integration time, in SAR focusing, is lower bounded by the requirement on a large time $\times$ bandwidth product, TBP

$$TBP = T_o \times B_D = T_o \times v_0/\rho_{az} > 1. \tag{29}$$

In a geostationary geometry, this constraint becomes critical, requiring a more robust approach. In particular, we notice from the top figure of Fig. 6 that the decrease in coherence due to a reduction of the subaperture time T_s is much steeper than the one due to its increase. This implies that the impact of spatial broadening of the resolution cell is dominant over temporal fluctuations. This effect can be mitigated by applying a smooth window to the subapertures rather than a rectangular one.

The numerical computation of coherence enables both the evaluation of different window shapes and the optimization of the subaperture duration. The bottom figure of Fig. 6 shows that using a Hamming window provides a significant improvement in coherence and the extent of the optimal integration time, thereby relaxing the requirement on the time–bandwidth product. It can be inferred that, under optimal conditions for the two windows, approximately 40 s for the boxcar and 80 s for the Hamming, the TBPs are nearly 0.4 and 1.5, respectively, meaning that the lower bound of 1 is satisfied only for the Hamming window. The increase in the optimal integration time associated with the Hamming window is inherent to the functional characteristics of the window itself. While the Hamming window effectively suppresses sidelobe levels, it simultaneously broadens the main lobe, thereby degrading azimuth resolution. Consequently, to maintain target-resolution performance, a proportional increase in the synthetic aperture length is required. It follows that the degree of resolution degradation introduced by a specific window function is directly correlated with the required optimal integration time. The performance is sensitive to the choice of the subaperture length. As shown in Fig. 6, for short subapertures, coherence is primarily limited by the spatial decorrelation of the troposphere. In this regime, the coherence exhibits a steep decline, indicating that performance degrades rapidly as integration time decreases. Conversely, for long subapertures, temporal decorrelation becomes dominant, and the coherence smoothly approaches an asymptote. These results demonstrate that employing longer integration times can provide more robust performance when the optimal parameters are not known.

Although the approximated expression in (27) tends to overestimate coherence, the optimal synthetic aperture time derived from (27) and evaluated in (28) closely matches the exact value, as shown in Fig. 6. Consequently, it can be reliably used to determine the optimal subaperture size for a rectangular window.

In order to verify the coherence model so far introduced, we run a Monte Carlo simulation, similar to the one described for the point target analysis, but assuming a distributed target and optimal integration time. The results are plotted in Fig. 7 as

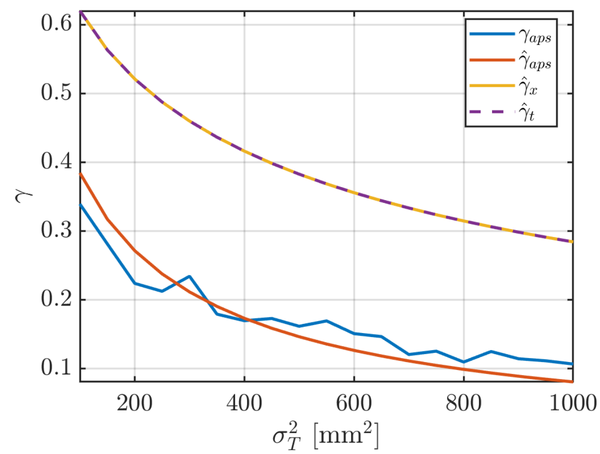

Fig. 7. Coherence between APS-free and APS-corrupted images with respect to the tropospheric variogram sill value computed by assuming the optimum subaperture time and 16 m/s of velocity. The four curves represent the temporal (dotted), spatial (yellow), and total coherence (red), computed according to the approximated model, and are compared with the results of a Monte Carlo estimation (blue).

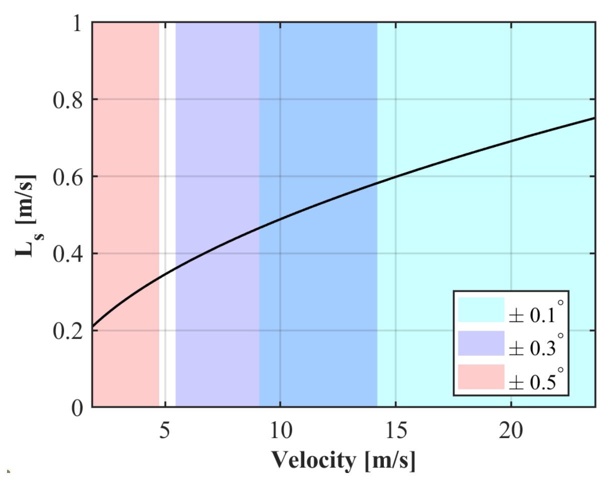

Fig. 8. Optimal subaperture extent as a function of the velocity.

a function of atmospheric turbulence, assuming a rectangular window—which is not optimal nor recommended but which allows us to verify the goodness of the simple approximation provided by (27). Statistics have been evaluated by averaging over $N_r = 1000$ range lines, under the assumption that every range line is subjected to the same atmosphere but with a different random source. The estimated coherence is fairly consistent with the theoretical model. The approximated formulation is no longer valid when a Hamming window is applied; therefore, the exact numerical model is required to correctly evaluate this configuration. Crucially, our exact analysis demonstrates that applying a Hamming window improves coherence and yields an optimal aperture length approximately twice the theoretical value.

In Fig. 8, the values of the optimal synthetic aperture are plotted as a function of velocity over the range relevant to geostationary orbits. The resulting coherence is shown in Fig. 9. Velocity ranges corresponding to different orbital eccentricities are indicated by shaded regions. Note that the

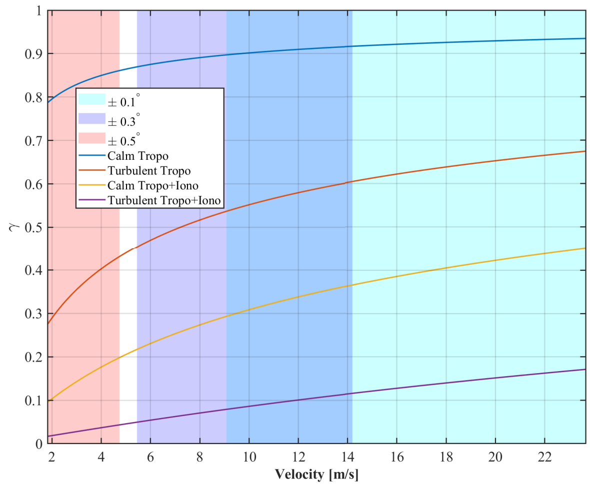

Fig. 9. Coherence between APS-free and APS-affected images with respect to the velocity in different atmospheric conditions.

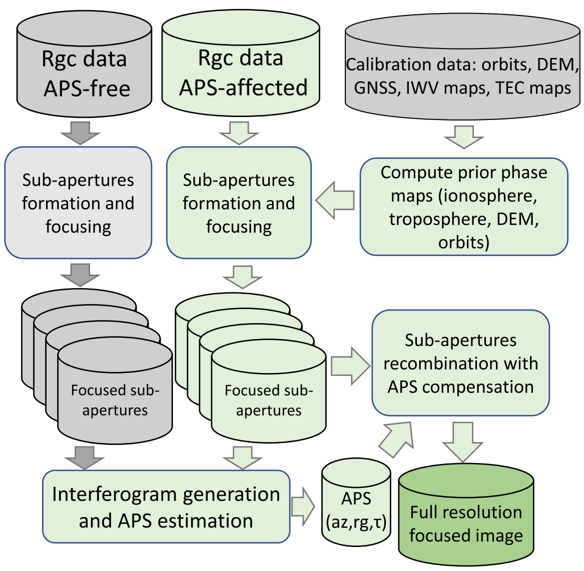

Fig. 10. Schematic block diagram for focusing of APS-affected data.

background ionosphere has a significant impact on the system design.

IV. Compensation of APS and System Performance

So far, we have shown that the spatiotemporal variability of the APS significantly hinders the generation of high-quality images, affecting both azimuth resolution and coherence. The quality can, however, be recovered by estimating the APS and then compensating for it during the focusing process. The final performance will then depend on the accuracy of the estimated APS phase.

The method assumed here for focusing that embeds APS estimation and compensation is based on interferometric autofocusing, as shown in Fig. 10. This approach is well established in the literature, with variants proposed in [28], [33], [47], and [59]. The purpose of this work is to assess the final focusing quality in the presence of ionospheric and atmospheric effects using the optimal approach proposed here and to provide a quantitative performance assessment based on the statistical analysis presented in Appendices A and B.

The accuracy of the estimated APS phase can be derived by considering that, for each range and azimuth position r_0, x_0 inside a subaperture interferometric pair, we estimate the APS $\phi_{APS}(r_0, x_0; \tau_s)$ by averaging nearby samples of the interferogram. When dimensioning the estimation window, one must consider that the APS decorrelates with space. The coherence contribution of the APS for two samples at a distance Δ_x can be computed by assuming a normal distribution of the APS phase

$$\begin{aligned}\gamma_{APS}(\Delta_x) &= E\left[\exp(j\phi_a(x_0))\cdot\exp(-j\phi_a(x_0+\Delta_x))\right]\\ &= \exp\left(-\frac{\sigma^2_{\phi a}\cdot\Delta_x}{2}\right)\\ &= \exp\left(-\frac{\sigma^2_{0_T}}{\cos^2\theta}\frac{|x|}{x_T}\right)\end{aligned}\tag{30}$$

where the last expression has been derived by the tropospheric variogram (2) computed at time lag $\tau = 0$. In Appendix C, the Cramér–Rao bound (CRB) for the estimation of the interferometric SAR phase is derived for the case of exponential decorrelation

$$\begin{aligned}\sigma_\phi &= \sqrt{\frac{1-\gamma^2}{2N_{eq}\gamma^2}}\\ \gamma &= \gamma_0\cdot\gamma_{APS}\cdot\gamma_{SNR}\end{aligned}\tag{31}$$

where the total coherence, γ, has been expressed as the product of one due to APS, γ_{APS} in (30), one due to signal-to-noise ratio, γ_{SNR}, and one term, γ_0, which accounts for all the other decorrelation sources, mostly temporal decorrelation, already analyzed in [20]. The equivalent number of looks N_{eq} is computed according to the expression in Appendix C

$$N_{eq} = 0.28\cdot\frac{\rho_{la}}{\rho_{az}\rho_{gr}}\tag{32}$$

where ρ_{la} is the area of the estimation window, whose size is the APS decorrelation interval x_T^2, and ρ_{az} and ρ_{gr} are the range and azimuth resolution of the focused data.

A. Performance Optimization

The standard deviation of the estimated phase is the primary performance metric in SAR interferometry and, in our case, the key driver for estimating the APS. To optimize this quantity, we note that it depends directly on the signal-to-noise ratio (SNR) through the coherence γ_{SNR} in (31) but also indirectly on the range resolution.

As the range resolution becomes finer, the equivalent number of looks Neq increases, but the SNR degrades. These two effects act in opposition with respect to the phase estimation accuracy, implying that an optimal trade-off—and consequently an optimal range resolution—can be derived.

TABLE II
SYSTEM PARAMETERS

γ_0	0.5
η	-3.8 dB
N_0	-193.83 dB
G	48 dB

In order to find the optimum, let us express γ_{SNR} as

$$\gamma_{SNR} = \frac{1}{1 + \frac{\sigma_N}{\sigma_0}} \tag{33}$$

where σ_N and σ_0 represent the backscatter coefficient of thermal noise and the scene, and their ratio is the inverse of the SNR.

The thermal noise, or noise equivalent sigma zero (NESZ), can be related to the range resolution, ρ_{gr}, the mean transmitted power P_m, and the other radar parameters through the radar equation [14]

$$\text{SNR} = \frac{P_m G^2 \lambda^2 \eta \rho_{az} \rho_{gr} T_s}{(4\pi)^3 R_0^4 N_0} \cdot \sigma_N = 1 \rightarrow \sigma_N = \frac{K_p}{\rho_{gr}}$$
$$K_p = \frac{(4\pi)^3 R_0^4 N_0}{P_m G^2 \lambda^2 \eta \rho_{az} T_s}. \tag{34}$$

In (34), we have evidenced that NESZ is inversely proportional to the range resolution through the term K_p. This implies that we can evaluate the optimal σ_N by minimizing σ_ϕ in (31) and combining with (32) and (34)

$$\arg\min_{\sigma_N} \left(\sigma_\phi^2\right) = \arg\min_{\sigma_N} \left(\frac{1-\gamma^2}{\gamma^2} \cdot \frac{\rho_{az} \cdot \rho_{gr}}{2\rho_{la}}\right). \tag{35}$$

The minimization can be carried out formally by replacing ρ_{gr}, from (34), and γ from (33)

$$\arg\min_{\sigma_N} \left(1 - \frac{\gamma_0^2 \gamma_{APS}^2}{(1 + \sigma_N/\sigma_0)^2}\right) \cdot \left(\frac{1}{\sigma_N} + \frac{2}{\sigma_0} + \frac{\sigma_N}{\sigma_0^2}\right). \tag{36}$$

The exact closed-form solution is not simple, but, by noticing that $\gamma \ll 1$ by including all the decorrelation sources, we easily get the near optimum

$$\arg\min_{\sigma_N} \left(\frac{1}{\sigma_N} + \frac{\sigma_N}{\sigma_0^2}\right) \rightarrow -\frac{1}{\sigma_N^2} + \frac{1}{\sigma_0^2} = 0 \rightarrow \sigma_N = \sigma_0. \tag{37}$$

This means that the optimum SNR should be unitary, and then, $\gamma_{SNR} = 0.5$, which, in turn, confirms the approximation above.

Given the optimal values of SNR and resolution, we can compute the accuracy of the estimated phase under different orbit (velocity) and power conditions and, based on that, assess the mission's feasibility. The analysis is carried out by keeping γ_0 fixed and by assuming the parameters listed in Table II.

By combining (31), (32), (33), and (37), σ_ϕ can be expressed as a function of γ_0, v_0, and P_m

$$\sigma_\phi(P_m, v_0, \gamma_0) = \sqrt{\frac{1 - 0.25\gamma_0^2\gamma_{APS}^2(v_0)}{2\frac{0.28 \cdot x_T^2}{\rho_{az}(v_0)\cdot\rho_{gr}(P_m, v_0)} 0.25\gamma_0^2\gamma_{APS}^2(v_0))}}. \tag{38}$$

Fig. 11 shows the values of the standard deviation of the estimated APS, σ_ϕ, as a function of the average transmitted power for the sensors' velocities allowed by ITU regulations.

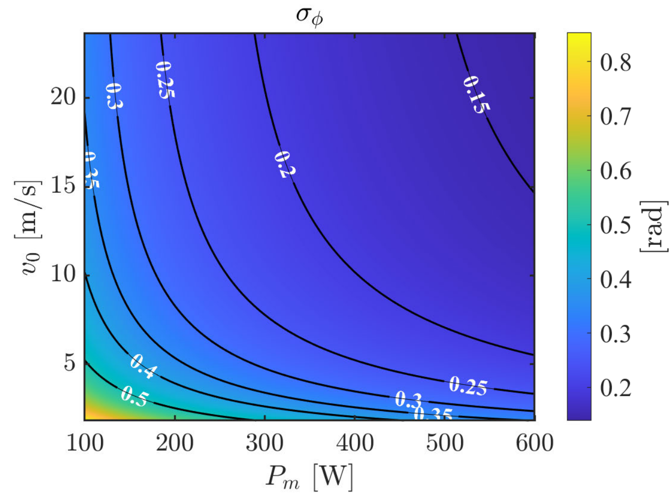

Fig. 11. Standard deviation of the estimated APS as a function of average transmitted power and the sensor velocity.

It is clear that the higher the power and the velocity, the better the performance. Consequently, using orbital velocities corresponding to ITU longitudinal extensions of ±0.5° results in a significant reduction of σ_ϕ.

V. APS Estimation and Compensation: Simulations

In long apertures typical of NZI GEO-SAR systems, decorrelation induced by the troposphere and, more critically, by the ionosphere becomes significant. Therefore, the estimation and compensation strategy relies on multiple subapertures, following the approaches proposed in [28] and [60].

The estimation and compensation procedure is illustrated in Fig. 10. The performance of the proposed method is assessed through simulations in a scenario in which the atmosphere is the only source of decorrelation. The objective is to evaluate the interferometric phase accuracy, the final azimuth resolution, and the resulting coherence.

In the simulation, the satellite velocity is fixed at 16 m/s, and the total integration time is set to 1 h, yielding a nominal azimuth resolution of 18 m. To improve the atmospheric estimation accuracy, 1000 range lines are averaged. The scene reflectivity is modeled as a complex Gaussian random process with dimensions $[N_x \times N_r]$. Each subaperture is centered at every slow-time sample, maximizing the overlap between consecutive subapertures and preventing information loss. Since the atmosphere is assumed to be the only decorrelation source, thermal noise and external decorrelation effects are not considered. A Hamming window is applied, as it provides better performance, as discussed in the previous sections. In Algorithm 1, the pseudocode for the estimation and compensation method is reported.

In the case of a single subaperture, (38) can be validated by estimating only the spatial component of the APS and evaluating the accuracy in this 1-D scenario. This is achieved by computing the standard deviation of the residual phase error between the true APS, evaluated at the aperture center, and the interferometric phase. For this validation, a single range line

Algorithm 1 Subaperture Focusing and APS Estimation

Require: Reference signal $\mathbf{s}$, phase matrices $\mathbf{\Phi_R}, \mathbf{\Phi_T}, \mathbf{\Phi_I}$, grid dimensions N_τ, N_x, N_r, sub-aperture integration time T_o, and temporal step $\Delta\tau$

Ensure: Interpolated estimated APS phase $\hat{\boldsymbol{\phi}}_{APS}$

1: Compute half sub-aperture size $N_{ss}^{half} = \lfloor T_o/(2\Delta\tau) \rfloor$
2: Define sub-aperture centers $\mathcal{C} = \{c_1, c_2, \ldots, c_{N_s}\}$ with unitary step size
3: **for** each sub-aperture $k \in \{1, \ldots, N_s\}$ **do**
4: Extract slow-time indices for the k-th center: $i_{sat} = (c_k - N_{ss}^{half}, \ldots, c_k + N_{ss}^{half})$
5: Generate normalized Hamming window $\mathbf{W}^{(k)}$ over the i_{sat}
6: Compute the k-th focused data without APS through (17)
7: Compute the k-th focused data with APS through (9)
8: Compute the k-th interferometric product $\mathbf{I^{(k)}}$
9: Calculate the mean along the range dimension:

$$\mathbf{I^{(k)}} = \frac{1}{N_r} \sum_{r=1}^{N_r} \mathbf{I^{(k)}}(:, r)$$

10: Extract total sub-aperture phase estimations
11: Interpolate the estimated APS phasor to the original grid size N_τ
12: Extract final interpolated phase $\hat{\boldsymbol{\phi}}_{APS}$:

is considered, and the results are averaged over 1000 Monte Carlo realizations.

By adapting (38) to the considered case (1-D azimuth and atmospheric decorrelation only) and using the parameters reported in Table I under normal atmospheric conditions and optimal integration time, the theoretical phase accuracy is 0.58 rad. The phase accuracy estimated from the simulation is 0.61 rad, showing excellent agreement with the theoretical prediction. The minor discrepancy can be attributed to the equivalent number of looks and the azimuth resolution, which is ideally computed using (4), without accounting for the effects of the windowing function and the APS.

Once the APS is estimated for each subaperture, the full-resolution APS is reconstructed by interpolating the estimates onto the original grid. The reconstructed APS is then subtracted from the true APS, yielding the compensated signal.

A representative atmospheric scenario is simulated using the parameters reported in Table I under normal atmospheric conditions. In this case, the optimal subaperture integration time is approximately 40 s. However, as shown in Fig. 6, when a Hamming window is applied, the optimal integration time is approximately twice the theoretical value. Consequently, an integration time of 80 s is adopted for each subaperture. Given the high variability of the atmosphere, a Monte Carlo approach has been carried out by applying the APS compensation algorithm proposed in Section IV over 100 realizations.

Fig. 12 shows an example of APS estimation results. The residuals between the total APS and the estimated APS are shown in Fig. 13.

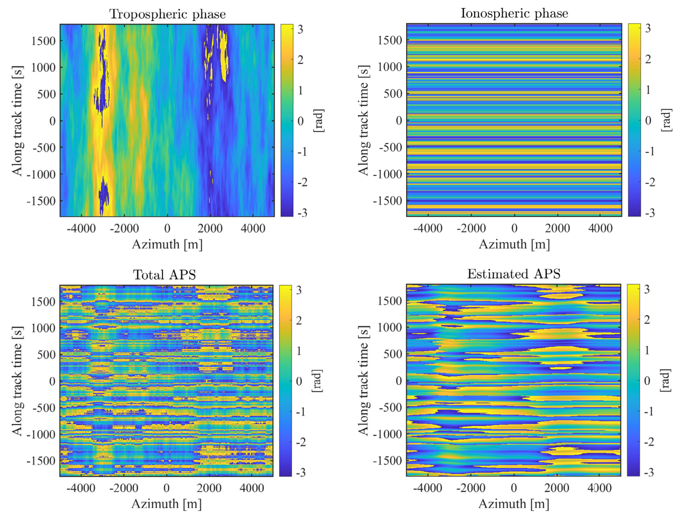

Fig. 12. Simulated APSs. (Top-left) Tropospheric phase. (Top-right) Ionospheric phase. (Bottom-left) True APS (wrapped). (Bottom-right) Estimated APS (wrapped).

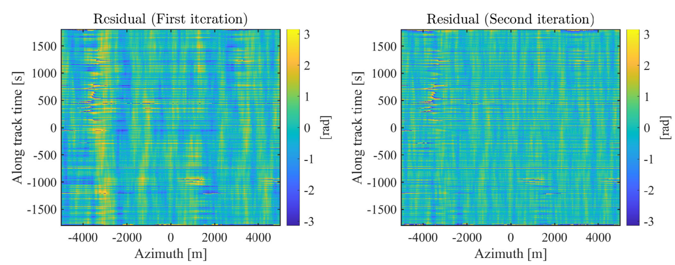

Fig. 13. Residuals between total and estimated APS after (left) one iteration and (right) two iterations.

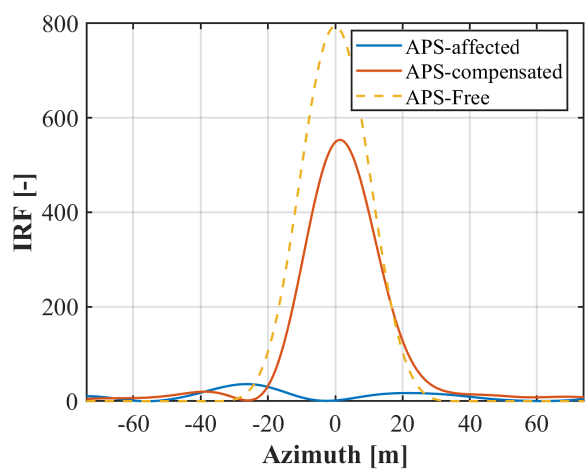

Fig. 14. IRF after APS compensation compared to APS-free and APS-affected cases. The satellite velocity is 16 m/s, and the total integration time is 1 h. The other parameters are reported in Table I, assuming normal tropospheric conditions. A Hamming window is applied.

A. Impulse Response Function

By assuming a single impulsive target in the center of the scene, as in Section III-C, the IRF in (10) is evaluated in the case of the compensated signal.

In Fig. 14, where an example of a single realization is represented, a significant performance improvement is observed.

The central lobe is clearly reconstructed, unlike in the APS-affected case (single realization), and the nominal azimuth resolution is almost recovered. Under APS-free conditions, the nominal azimuth resolution is 18 m. The application of a Hamming window slightly degrades this value to 24 m. After applying the compensation procedure, the final achieved azimuth resolution is 25 m.

B. Distributed Target

In the case of the distributed target described in Sections III-D and III-E, the coherence between the two signals after the APS compensation procedure is evaluated. The compensated focused data are expressed as

$$\hat{\mathbf{s}}_{\text{APS},c} = \mathbf{\Phi}_R^H \left(\mathbf{\Phi}_R \odot \mathbf{W} \odot \mathbf{\Phi}_T \odot \mathbf{\Phi}_I \odot \hat{\mathbf{\Phi}}^*_{\text{APS}}\right)\mathbf{s} \tag{39}$$

where $\hat{\mathbf{\Phi}}^*_{\text{APS}}$ denotes the complex conjugate of the estimated APS phasor $e^{j\hat{\phi}_{\text{APS}}}$ and $\hat{\phi}_{\text{APS}}$ is the estimated total atmospheric phase. The coherence is then computed using (16) applied to the compensated focused data in (39)

$$\gamma_{APS,c} = \frac{\mathrm{tr}\left(\hat{\mathbf{s}}\hat{\mathbf{s}}_{APS,c}^{H}\right)}{\sqrt{\mathrm{tr}\left(\hat{\mathbf{s}}\hat{\mathbf{s}}^{H}\right)\cdot \mathrm{tr}\left(\hat{\mathbf{s}}_{APS,c}\hat{\mathbf{s}}_{APS,c}^{H}\right)}}. \tag{40}$$

The mean value of the coherence after the APS compensation computed using (40) over the Monte Carlo simulation is 0.75 with a standard deviation of 0.027. This represents a significant improvement compared to the coherence value of 0.05 (standard deviation of 0.03) obtained in the uncompensated case.

The proposed method demonstrates strong performance, achieving a final coherence of 0.75. To further refine these results, an iterative strategy was investigated, specifically by doubling the subaperture length to enhance the resolution of each subimage. Experimental results indicate that this doubling strategy yields superior performance, with a final coherence of 0.84. The residual standard deviation decreases from 0.84 rad after the first iteration to 0.70 rad after the second. These results were obtained without applying any azimuth multilook, representing a worst case scenario for the estimation process. Even under these conditions, the standard deviation remains below 1 rad, indicating robust performance. This is further verified by evaluating the Cramér–Rao bound (CRB) in this scenario

$$\sigma_{\phi_{CRB}} = \sqrt{\frac{1-\gamma^2_{APS,c}}{2\gamma^2_{APS,c}}}. \tag{41}$$

After the first iteration, the CRB calculated using (41) is 0.62 rad, which validates our results as being close to the theoretical lower bound. Furthermore, after the second iteration, the estimation accuracy approaches this bound, suggesting that further iterations would yield only marginal performance improvements.

VI. Conclusion

The joint contribution of tropospheric and ionospheric phase screens has been identified as a key driver in the feasibility assessment and system design of an NZI geosynchronous SAR. A stochastic model has been developed to account for the overall APS, and a numerical approach has been introduced to quantify its impact on the mean and standard deviation of a focused point target, as well as on coherence loss for distributed targets. The proposed model has been used to optimize the subaperture window shape and duration, and to evaluate the accuracy of APS estimation via interferometric autofocusing.

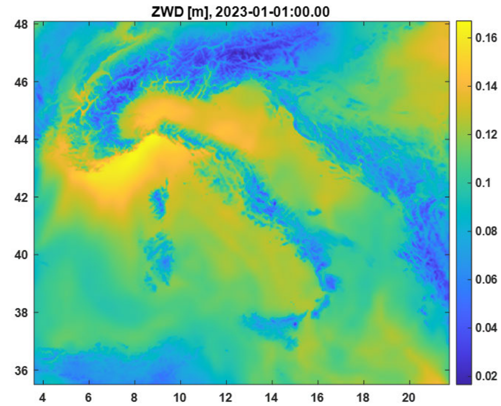

Fig. 15. ZWD over Italy at 00:00 on January 1, 2023.

The actual performance has been evaluated under realistic conditions by exploiting large datasets to retrieve ionospheric and tropospheric variogram parameters.

All the results have been supported by simulations.

The feasibility of the geostationary mission depends on the platform velocity and the available power. Results are presented for the C-band, but they can be readily extended to other frequencies.

The final conclusion is that, if the orbit is constrained within the ±0.1° ITU box, the mission is feasible, but the performance is not optimal. In contrast, a box five times wider—still compliant with ITU regulations for experimental platforms—provides significantly improved performance.

Appendix A

The quantitative assessment of the spatial and temporal variabilities of water vapor is crucial for evaluating the performance of long-integration SAR systems, such as geostationary SAR operating at the C-band and higher frequencies. The variogram model in (2) was first introduced in [41] as an extension of the temporal and spatial power laws, which are well established in the literature [61], [62], [63], [64].

The verification and quantification of this variogram model are nowadays enabled by the generation of high-resolution weather models. For the present analysis, we rely on zenith WD (ZWD) data covering an entire year (2023) over the 1000 × 1000 km domain shown in Fig. 15.

These ZWD fields were derived from a WRF model with a temporal resolution of 1 h and a spatial resolution of 1.5 × 1.5 km. WRF is a mesoscale forecasting system that solves the nonhydrostatic, fully compressible Euler equations on an Arakawa-C grid with mass-based terrain-following

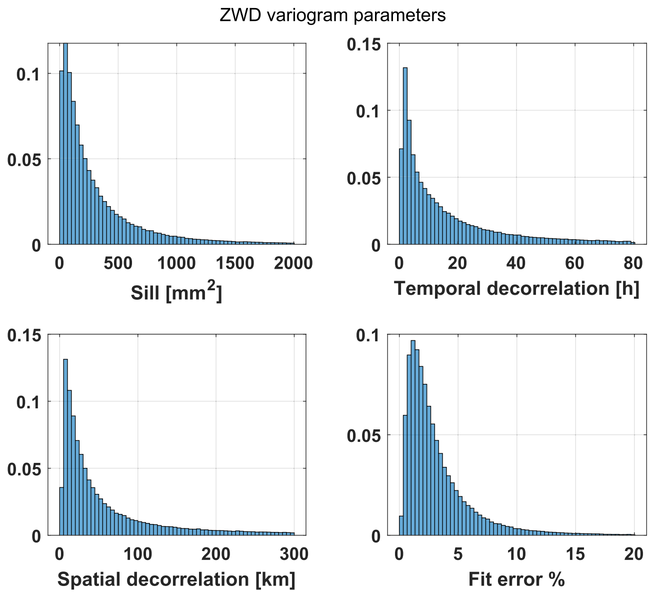

Fig. 16. Histograms of tropospheric variogram parameters and fit error, estimated over 200 000 variograms in the entire year 2023.

coordinates. It is designed for both research and operational applications and supports spatial resolutions ranging from hundreds of meters to hundreds of kilometers [65].

The WRF configuration adopted here employs three nested domains with horizontal resolutions of 13.5, 4.5, and 1.5 km and includes the following physical parameterizations. The Yonsei University scheme [66] is used for planetary boundary layer turbulence closure; the RRTMG shortwave and longwave radiation schemes [67], [68], [69] are applied for radiative transfer; and the rapid update cycle (RUC) multilevel soil model (six levels: 0, 5, 20, 40, 160, and 300 cm) [70], [71] is used for land–surface processes. For consistency with the GFS initial and boundary conditions, the New Simplified Arakawa–Schubert convection scheme [72] is activated only in the outermost domain (13.5 km), while the two inner domains (4.5 and 1.5 km) do not employ a cumulus scheme, as their grid spacing allows explicit resolution of convection. The model outputs have been validated seasonally, and the rainfall forecast performance has also been compared with that of another limited area model over one year to assess predictive capability [73]. An example ZWD map is shown in Fig. 15.

The fitting process has been carried out by estimating variograms in the space–time domain, limited to the land masses, since SAR cannot provide water vapor maps over the sea. In the entire year, over 200 000 variograms were generated and fit for the three parameters involved in (2): the space and time decay, x_T and τ_T, and the sill σ_T^2.

The parameter histograms are shown in Fig. 16, together with the normalized fitting error, which is defined as

$$\epsilon = \frac{\iint \left(V_{T,E}(\tau,x) - V_T(\tau,x)\right)^2 \, d\tau\, dx}{\iint \left(V_{T,E}(\tau,x)\right)^2 \, d\tau\, dx} \tag{42}$$

where $V_{T,E}(\tau, x)$ is the empirical semivariogram and $V_T(\tau, x)$ is the fit model.

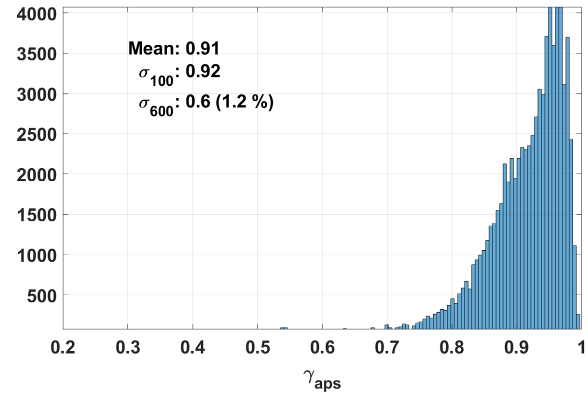

Fig. 17. Histogram of coherence estimated using (27) with v_0 = 14.2 m/s.

TABLE III
SEASONAL EQUIVALENT SILL VALUES [MM^2] FOR NORMAL AND STRONG TURBULENCES

	Normal turbulence	Strong turbulence
Spring	100	400
Summer	210	750
Autumn	100	500
Winter	50	250
All	100	550

As shown, there is a considerable spread across all three parameters. However, for the present analysis, it is necessary to define representative ”normal” and ”turbulent” conditions.

To this end, a set of 200 000 fit variogram parameter triplets was used to evaluate the coherence, γ_{APS}, according to (27), and assuming that $\theta = 50°$ and $v_0 = 16$ m/s. The resulting coherence histogram is shown in Fig. 17. The mean value reported therein is very close to the coherence obtained using the parameter set $\sigma_T^2 = 100$ mm^2, $\tau_T = 10$ h, and $x_T = 10$ km, as recommended in the literature [2], [31], [41], [48]. This confirms the consistency with previously reported ”normal” atmospheric conditions.

For strong turbulence conditions, the same parameter set yields a coherence value close to the lower bound of the histogram in Fig. 17, supporting its use as a conservative reference.

For further insight, the values of σ_T^2 corresponding to the median and 5th percentile of the seasonal WRF-based analysis are reported in Table III as recommended for ”Normal” and ”Strong” turbulences.

APPENDIX B

Historical nowcastings of the total electron content (TEC) over the Mediterranean area are provided by the eSWua database [52], developed by INGV. These maps contain VTEC values derived from GNSS measurements, sampled every 5 min with a 1-min integration time, and gridded at a spatial resolution of 0.5° × 0.5°. The dataset covers Europe from 10° W–45° E and 30° N–76° N. Owing to their continuous temporal coverage, these maps enable the monitoring of large-scale, slowly varying ionospheric structures that introduce continuous and systematic phase delays in the C-band radar

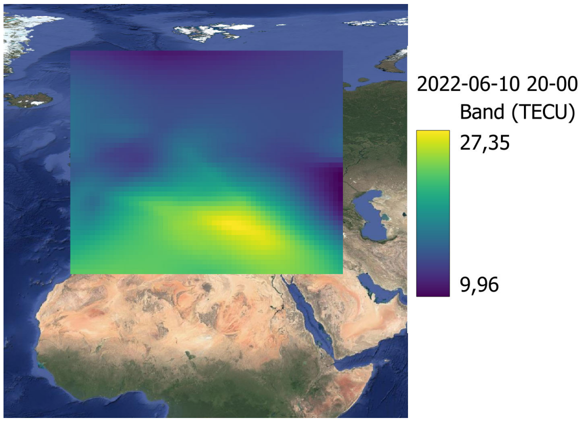

Fig. 18. Example of VTEC nowcasting over Europe.

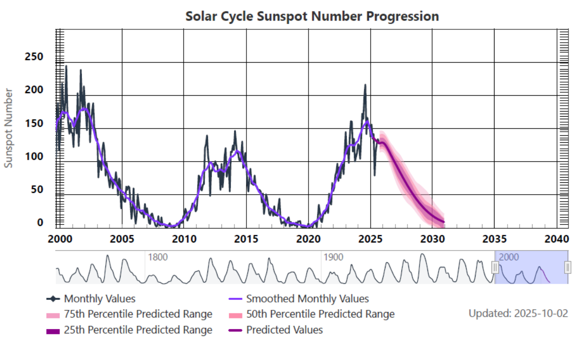

Fig. 19. Solar activity from the year 2000 to the present. Data source: WDC-SILSO, Royal Observatory of Belgium, Brussels [76].

TABLE IV

SEASONAL AVERAGE DISTANCE FOR 1-TECU VARIATION

Season	Latitude [km]	Longitude [km]
Spring	100	190
Summer	150	250
Autumn	120	200
Winter	180	270

signals [51]. This aspect is especially relevant for GEO-SAR, where the long integration times required for data acquisition preclude neglecting background ionospheric variability. Conversely, rapid and localized scintillation effects—although less significant at mid-latitudes [51], [74]—are not considered in this work.

Since TEC dynamics exhibit partially predictable behavior, ionospheric forecasting models may be used to compensate for background effects; however, the residual error from such predictions still needs to be accounted for. An example of an eSWua VTEC map is shown in Fig. 18. To extract background variability statistics, VTEC data from December 2021 to November 2022—corresponding to medium solar activity within Solar Cycle 25 (2019–2030)—were analyzed. This cycle is expected to peak in 2025, as illustrated in Fig. 19 [75].

Background TEC exhibits both spatial and temporal variabilities. Spatial variations are strongest near tropical and polar latitudes and are smallest at mid-latitudes [77], where

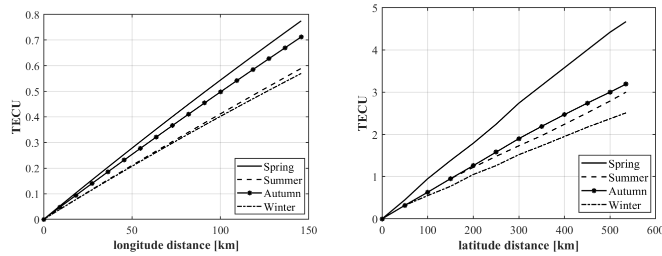

Fig. 20. Seasonal spatial averages of VTEC variograms over the Mediterranean region. (Left) Along longitude and (right) latitude.

TABLE V

AVERAGE LONGITUDINAL VTEC RATE

Season	Rate [TECU/km]
Spring	0.0049
Summer	0.0038
Autumn	0.0046
Winter	0.0035

most NZI GEO-SAR acquisitions will be conducted. Due to the large-scale nature of ionospheric structures, spatial variability was evaluated first in latitude and then in longitude. A total of 500 000 spatial variograms were computed up to a lag of 500 km, and the empirical distances corresponding to a 1-TECU variation were extracted for different seasons and directions. Table IV summarizes these distances, while Fig. 20 shows the seasonal average longitudinal and latitudinal variograms. Spring exhibits the largest variability. Overall, however, these spatial gradients remain modest and are not expected to degrade subaperture focusing. The corresponding linear rates in VTEC for each season are reported in Table V.

In contrast, temporal variations were found to dominate, with fluctuations reaching 1 TECU within minutes. Since these variations exceed the spatial component during SAR focusing, the temporal variogram was used to model ionospheric variability for the algorithm presented in Section III. From the dataset, 20 000 temporal variograms with time lags up to 1 h were computed over six subregions, defined by three latitudinal and two longitudinal bands. A suitable approximation for the expected variability of the TEC at zenith is given by the linear model

$$2V_{\mathrm{TEC}}(\tau) = \mathbb{E}\left[|\mathrm{VTEC}(t+\tau) - \mathrm{VTEC}(t)|^2\right] = \frac{|\tau|}{\alpha_{\mathrm{TEC}}} \tag{43}$$

where τ is the time lag, θ is the GEO-SAR incidence angle, and α_{TEC} is the increase-rate parameter, expressed in s/TECU^2. The incidence angle factor was not used during the fitting of VTEC values but is included here for SAR propagation modeling.

The fitting error was computed as in (42). Examples of fit variograms are shown in Fig. 21, and the distributions of fitting parameters for the summer season are given in Fig. 22. Seasonal statistics are reported in Table VI. Median fit errors are only a few percent, consistent with the Kolmogorov turbulence model for the ionosphere [54]. The expected variability of the

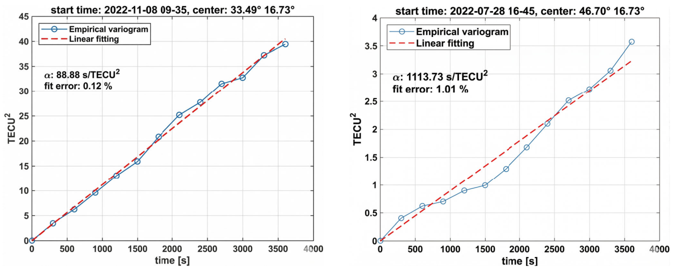

Fig. 21. Empirical VTEC variograms and corresponding linear fits.

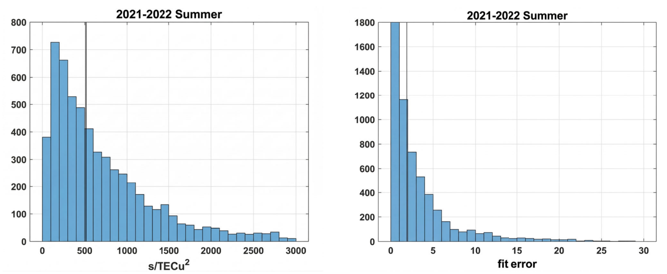

Fig. 22. Histogram of variogram fitting parameters for (left) summer 2022 and (right) corresponding fitting error.

TABLE VI

SEASONAL TEMPORAL STATISTICS OF α_{TEC}

Season	Mean [s/TECU^2]	Mean error (%)	Median [s/TECU^2]	Median error (%)
Spring	479.4	4.69	308.7	2.99
Summer	698.4	3.31	513.5	1.89
Autumn	523.4	3.62	341.3	2.30
Winter	755.5	5.00	550.5	2.92

TABLE VII

SEASONAL MEDIAN VALUES OF α_{LOS} AT 16.73° E

	θ	α_{LOS}
Spring		
46.70°N	54°	205.7
40.09°N	47°	153.0
33.49°N	43°	55.9
Summer		
46.70°N	54°	319.4
40.09°N	47°	241.4
33.49°N	43°	97.9
Autumn		
46.70°N	54°	247.5
40.09°N	47°	153.2
33.49°N	43°	73.5
Winter		
46.70°N	54°	327.7
40.09°N	47°	285.3
33.49°N	43°	139.3

TEC in the line of sight (LOS) is expressed as

$$2V_{\text{TEC}_{\text{LOS}}}(\tau) = \frac{|\tau|}{\alpha_{\text{TEC}}\cos^2\theta} = \frac{|\tau|}{\alpha_{\text{TEC}_{\text{LOS}}}} \tag{44}$$

where α_{LOS} is the ionospheric increase-rate parameter in LOS. Spatial variations of α_{LOS} across the three subregions are reported in Table VII.

As illustrated, the equinox seasons exhibit the greatest variability, and similar trends are observed at lower latitudes closer to the tropics. For the compensation algorithm, the overall median value of Table VI, $\alpha_{\text{TEC}} = 428$ s/TECU^2, was adopted. This corresponds to a single-pass propagation delay variance rate of $\alpha_I = 0.44$ mm^2/s at nadir, as shown in Fig. 23. The ionospheric delay variogram used in Section II-B is parameterized accordingly.

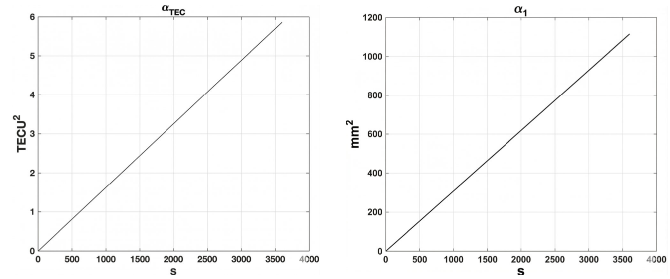

Fig. 23. (Left) Median VTEC variance rate ($\alpha_{\text{TEC}} = 428$ s/TECU^2) and (right) corresponding single-pass propagation delay.

APPENDIX C
ML ESTIMATION OF THE INTERFEROMETRIC PHASE

We derive here the maximum likelihood (ML) optimal phase estimator for the case of two interferometric vectors with known coherence, as in the atmospheric variogram.

We model the reference and secondary observations over a local window, $\mathbf{u}$ and $\mathbf{v}$, as

$$\mathbf{u} = \mathbf{s}_1, \quad \mathbf{v} = \mathbf{s}_2\, e^{j\phi} \tag{45}$$

where $\mathbf{s}_1$ and $\mathbf{s}_2$ are $[N \times 1]$ column vectors representing the underlying reflectivity in the two acquisitions and ϕ is the interferometric phase to be estimated.

We assume that the sources are zero-mean, complex circular Gaussian, mutually uncorrelated, with unit variance, and with a known diagonal cross-covariance

$$\mathbf{C}_s = \mathbb{E}\left[\mathbf{s}_1\mathbf{s}_2^*\right] = \text{diag}\left(\gamma_1, \ldots, \gamma_N\right) \tag{46}$$

where $(\cdot)^*$ denotes the Hermitian transpose. For the application of interest, all γ_n's are real.

We stack the two observations into the $[2N \times 1]$ vector

$$\mathbf{z} = \begin{bmatrix}\mathbf{u}\\ \mathbf{v}\end{bmatrix}.$$

The ML phase estimate ϕ_{ML} maximizes the conditional probability density of $\mathbf{z}$

$$f_{\mathbf{z}|\phi}\left(\mathbf{z}\,|\,\phi\right) \sim \mathcal{N}_c\left(\mathbf{0}, \mathbf{C}_z\right)$$

where $\mathcal{N}_c$ denotes the circular complex Gaussian distribution and $\mathbf{C}_z$ is the covariance matrix

$$\mathbf{C}_z = \begin{bmatrix}\mathbf{I}_N & \mathbf{C}_s e^{-j\phi}\\ \mathbf{C}_s e^{j\phi} & \mathbf{I}_N\end{bmatrix} \tag{47}$$

with $\mathbf{I}_N$ being the $N \times N$ identity matrix. All blocks in $\mathbf{C}_z$ are diagonal.

The ML estimate maximizes the log-likelihood

$$\phi_{\text{ML}} = \arg\max{}_{\phi}\left(-\mathbf{z}^*\mathbf{C}_z^{-1}\mathbf{z}\right) \tag{48}$$

since $\log|\mathbf{C}_z|$ is independent of ϕ.

The inverse covariance is also block-diagonal

$$\mathbf{C}_z^{-1} = \begin{bmatrix} \mathbf{G} & \mathbf{H} \\ \mathbf{H}^* & \mathbf{G} \end{bmatrix} \tag{49}$$

with

$$\mathbf{G} = \mathrm{diag}\left(\frac{1}{1-\gamma_1^2}, \ldots, \frac{1}{1-\gamma_N^2}\right)$$
$$\mathbf{H} = \mathrm{diag}\left(\frac{\gamma_1}{1-\gamma_1^2}, \ldots, \frac{\gamma_N}{1-\gamma_N^2}\right) e^{j\phi}.$$

By combining (48) and (49), we obtain

$$\phi_{\mathrm{ML}} = \arg\min_\phi \begin{bmatrix} \mathbf{u}^* & \mathbf{v}^* \end{bmatrix} \begin{bmatrix} \mathbf{G} & \mathbf{H} \\ \mathbf{H}^* & \mathbf{G} \end{bmatrix} \begin{bmatrix} \mathbf{u} \\ \mathbf{v} \end{bmatrix} \tag{50}$$

$$= \arg\min_\phi \left(2 \sum_{n=1}^{N} \left[g_n + h_n \,\Re\left(v_n u_n^* e^{-j\phi}\right)\right]\right) \tag{51}$$

where g_n and h_n denote the diagonal elements of $\mathbf{G}$ and $\mathbf{H}$, and $\Re$ is the real part.

By nulling the derivative of (51) with respect to ϕ, the ML phase estimate becomes

$$\phi_{\mathrm{ML}} = \arg\left\{\sum_{n=1}^{N} v_n u_n^* \frac{\gamma_n}{1-\gamma_n^2}\right\} \tag{52}$$

i.e., a coherence-weighted average of the interferometric samples $i_n = v_n u_n^*$. For constant coherence $\gamma_n = \gamma_0$, (52) reduces to the standard multilook phase estimator.

The estimation accuracy is bounded by the CRB. The Fisher information for ϕ is

$$F = -\mathrm{tr}\left(\frac{\partial \mathbf{C}_z}{\partial \phi} \frac{\partial \mathbf{C}_z^{-1}}{\partial \phi}\right).$$

The derivatives are

$$\frac{\partial \mathbf{C}_z}{\partial \phi} = \begin{bmatrix} \mathbf{0} & -j\mathbf{C}_s e^{-j\phi} \\ j\mathbf{C}_s e^{j\phi} & \mathbf{0} \end{bmatrix}$$
$$\frac{\partial \mathbf{C}_z^{-1}}{\partial \phi} = \begin{bmatrix} \mathbf{0} & -j\mathbf{H} e^{-j\phi} \\ j\mathbf{H} e^{j\phi} & \mathbf{0} \end{bmatrix}$$

and their product is

$$\frac{\partial \mathbf{C}_z}{\partial \phi} \frac{\partial \mathbf{C}_z^{-1}}{\partial \phi} = \begin{bmatrix} \mathbf{H}\mathbf{C}_s & \mathbf{0} \\ \mathbf{0} & \mathbf{H}\mathbf{C}_s \end{bmatrix}.$$

Hence, the Fisher information is

$$F = 2 \sum_{n=1}^{N} \frac{\gamma_n^2}{1-\gamma_n^2} \tag{53}$$

and the CRB becomes

$$\sigma_\phi^2 \geq \sigma_{\mathrm{CRB}}^2 = \left(2 \sum_{n=1}^{N} \frac{\gamma_n^2}{1-\gamma_n^2}\right)^{-1}. \tag{54}$$

For constant coherence $\gamma_n = \gamma_0$, this reduces to the classical result

$$\sigma_{\mathrm{CRB},0}^2 = \frac{1-\gamma_0^2}{2N\gamma_0^2}. \tag{55}$$

Consider now an exponential decorrelation model

$$\gamma_n = \gamma_0 \exp\left(-\frac{|x_n|}{x_T}\right) \tag{56}$$

and let N_{eq} be such that

$$\sum_{n=1}^{N} \frac{2\gamma_n^2}{1-\gamma_n^2} \simeq \frac{2N_{\mathrm{eq}}\gamma_0^2}{1-\gamma_0^2}. \tag{57}$$

If γ_0 dominates over the exponential term (i.e., $|x_n| \ll x_0$), then

$$N_{\mathrm{eq}} \simeq \sum_n \exp\left(-\frac{2\,|x_n|}{x_T}\right).$$

Approximating the sum over $-x_0 < x < x_0$ with spacing ρ_x yields

$$N_{\mathrm{eq}} \simeq 0.28\,\frac{2x_0}{\rho_x} = 0.28\,N_0 \tag{58}$$

where N_0 is the number of independent looks within a span of width $2x_T$.

Acknowledgment

This study was carried out within the Space It Up project. The authors would like to thank the anonymous reviewers for their constructive criticism and detailed, competent comments.

References

[1] R. Bamler and P. Hartl, "Synthetic aperture radar interferometry," *Inverse Problems*, vol. 14, no. 4, pp. 1–14, 1998.

[2] R. F. Hanssen, "Radar interferometry: Data interpretation and error analysis," in *Remote Sensing and Digital Image Processing*, vol. 2. Cham, Switzerland: Springer, 2001.

[3] F. De Zan and F. Rocca, "Coherent processing of long series of SAR images," in *Proc. IEEE Int. Geosci. Remote Sens. Symp.*, vol. 3, Jun. 2005, pp. 1987–1990.

[4] H. A. Zebker and J. Villasenor, "Decorrelation in interferometric radar echoes," *IEEE Trans. Geosci. Remote Sens.*, vol. 30, no. 5, pp. 950–959, May 1992.

[5] R. Bamler and D. Just, "Phase statistics and decorrelation in SAR interferograms," in *Proc. IEEE Int. Geosci. Remote Sens. Symp.*, Aug. 1993, pp. 980–984.

[6] A. Moussessian, C. Chen, W. Edelstein, S. Madsen, and P. Rosen, "System concepts and technologies for high orbit SAR," in *IEEE MTT-S Int. Microw. Symp. Dig.*, Jul. 2005, pp. 1623–1626.

[7] J. Matar, M. Rodriguez-Cassola, G. Krieger, and A. Moreira, "On the equivalence of LEO-SAR constellations and complex high-orbit SAR systems for the monitoring of large-scale processes," *IEEE Geosci. Remote Sens. Lett.*, vol. 21, pp. 1–5, 2024.

[8] K. Tomiyasu and J. L. Pacelli, "Synthetic aperture radar imaging from an inclined geosynchronous orbit," *IEEE Trans. Geosci. Remote Sens.*, vols. GE–21, no. 3, pp. 324–329, Jul. 1983.

[9] K. Tomiyasu, "Synthetic aperture radar in geosynchronous orbit," in *Proc. Antennas Propag. Soc. Int. Symp.*, vol. 16, 1978, pp. 42–45.

[10] L. Cazzani et al., "A ground based parasitic SAR experiment," in *Proc. IEEE Int. Geosci. Remote Sens. Symp.*, vol. 3, Jun. 1999, pp. 1525–1527.

[11] J. Ruiz-Rodon, A. Broquetas, E. Makhoul, A. Monti Guarnieri, and F. Rocca, "Nearly zero inclination geosynchronous SAR mission analysis with long integration time for Earth observation," *IEEE Trans. Geosci. Remote Sens.*, vol. 52, no. 10, pp. 6379–6391, Oct. 2014.

[12] *Station-Keeping in Longitude of Geostationary Satellites in the Fixed Satellite Service*, document ITU-R S.484-3, 1992.

[13] A. Monti Guarnieri, A. Broquetas, A. Recchia, F. Rocca, and J. Ruiz-Rodon, "Advanced radar geosynchronous observation system: ARGOS," *IEEE Geosci. Remote Sens. Lett.*, vol. 12, no. 7, pp. 1406–1410, Jul. 2015.

[14] M. Monti, A. M. Guarnieri, F. Pelliccia, and A. Renga, "Geostationary interferometric SAR: Orbit design and control implementation," *IEEE Trans. Geosci. Remote Sens.*, vol. 63, 2025, Art. no. 5211017.

[15] J. Nicolás-Álvarez et al., "Interferometric orbit determination system for geosynchronous SAR missions: Experimental proof of concept," *Remote Sens.*, vol. 14, no. 19, p. 4871, Sep. 2022.

[16] A. Monti Guarnieri and F. Rocca, "Options for continuous radar Earth observations," *Sci. China Inf. Sci.*, vol. 60, no. 6, Jun. 2017, Art. no. 060301.

[17] K. A. C. de Macedo, R. Scheiber, and A. Moreira, "An autofocus approach for residual motion errors with application to airborne repeat-pass SAR interferometry," *IEEE Trans. Geosci. Remote Sens.*, vol. 46, no. 10, pp. 3151–3162, Oct. 2008.

[18] S. Hobbs, C. Mitchell, B. Forte, R. Holley, B. Snapir, and P. Whittaker, "System design for geosynchronous synthetic aperture radar missions," *IEEE Trans. Geosci. Remote Sens.*, vol. 52, no. 12, pp. 7750–7763, Dec. 2014.

[19] C. Convenevole and S. E. Hobbs, "Method for estimating clutter limited geosynchronous synthetic aperture radar performance," in *Proc. Int. Radar Conf. (RADAR)*, Sep. 2019, pp. 1–6.

[20] A. Recchia, A. M. Guarnieri, A. Broquetas, and A. Leanza, "Impact of scene decorrelation on geosynchronous SAR data focusing," *IEEE Trans. Geosci. Remote Sens.*, vol. 54, no. 3, pp. 1635–1646, Mar. 2016.

[21] C. Hu, Z. Chen, Y. Li, X. Dong, and S. Hobbs, "Research progress on geosynchronous synthetic aperture radar," *Fundam. Res.*, vol. 1, no. 3, pp. 346–363, May 2021.

[22] A. Monti-Guarnieri, M. Manzoni, D. Giudici, A. Recchia, and S. Tebaldini, "Vegetated target decorrelation in SAR and interferometry: Models, simulation, and performance evaluation," *Remote Sens.*, vol. 12, no. 16, p. 2545, Aug. 2020.

[23] J. Kellndorfer et al., "Global seasonal Sentinel-1 interferometric coherence and backscatter data set," *Scientific Data*, vol. 9, no. 1, p. 73, Mar. 2022.

[24] A. Aguasca, A. Broquetas, J. M. Lopez-Sanchez, X. Fabregas, J. J. Mallorqui Franquet, and M. Mas, "Assessment of the impact of long integration time in geosynchronous SAR imagery of agricultural fields by means of GB-SAR data," *IEEE J. Sel. Topics Appl. Earth Observ. Remote Sens.*, vol. 17, pp. 1338–1347, 2024.

[25] M. Mas et al., "Monitoring corn crop height and growth rate with interferometric coherence," *IEEE J. Sel. Topics Appl. Earth Observ. Remote Sens.*, vol. 17, pp. 20041–20049, 2024.

[26] D. Bruno and S. E. Hobbs, "Radar imaging from geosynchronous orbit: Temporal decorrelation aspects," *IEEE Trans. Geosci. Remote Sens.*, vol. 48, no. 7, pp. 2924–2929, Jul. 2010.

[27] D. Li, M. Rodriguez-Cassola, P. Prats-Iraola, Z. Dong, M. Wu, and A. Moreira, "Modelling of tropospheric delays in geosynchronous synthetic aperture radar," *Sci. China Inf. Sci.*, vol. 60, no. 6, Jun. 2017, Art. no. 060307.

[28] A. M. Guarnieri, A. Leanza, A. Recchia, S. Tebaldini, and G. Venuti, "Atmospheric phase screen in GEO-SAR: Estimation and compensation," *IEEE Trans. Geosci. Remote Sens.*, vol. 56, no. 3, pp. 1668–1679, Mar. 2018.

[29] C. Hu, Y. Li, X. Dong, R. Wang, and D. Ao, "Performance analysis of L-band geosynchronous SAR imaging in the presence of ionospheric scintillation," *IEEE Trans. Geosci. Remote Sens.*, vol. 55, no. 1, pp. 159–172, Jan. 2017.

[30] L. Porcello, "Turbulence-induced phase errors in synthetic-aperture radars," *IEEE Trans. Aerosp. Electron. Syst.*, vols. AES–6, no. 5, pp. 636–644, Sep. 1970.

[31] A. Ferretti, C. Prati, and F. Rocca, "Permanent scatterers in SAR interferometry," *IEEE Trans. Geosci. Remote Sens.*, vol. 39, no. 1, pp. 8–20, Jan. 2001.

[32] T. Long, C. Hu, Z. Ding, X. Dong, W. Tian, and T. Zeng, *Geosynchronous SAR: System and Signal Processing*. Cham, Switzerland: Springer, 2018.

[33] C. Hu, Y. Tian, X. Yang, T. Zeng, T. Long, and X. Dong, "Background ionosphere effects on geosynchronous SAR focusing: Theoretical analysis and verification based on the BeiDou navigation satellite system (BDS)," *IEEE J. Sel. Topics Appl. Earth Observ. Remote Sens.*, vol. 9, no. 3, pp. 1143–1162, Mar. 2016.

[34] L. Kou, M. Xiang, X. Wang, and M. Zhu, "Tropospheric effects on L-band geosynchronous circular SAR imaging," *IET Radar, Sonar Navigation*, vol. 7, pp. 693–701, Jul. 2013.

[35] *The Coordination Between Satellite Networks Using Slightly Inclined Geostationary-satellite Orbits (GSOs) and Between Such Networks and Satellite Networks Using Non-inclined GSO Satellites*, document ITU-R S.743-1, 1992.

[36] A. Benoit, R. Jolivet, and B. Pinel-Puyssegur, "Correction of tropospheric effects in SAR interferometry: A comparison of ERA-interim, ERA-5 and HRES global atmospheric models," Istituto Nazionale di Geofisica eVulcanologia, Rome, Italy, Tech. Rep., 2019. [Online]. Available: https://doi.org/10.13127/eswua/tec

[37] J. L. Davis, T. A. Herring, I. I. Shapiro, A. E. E. Rogers, and G. Elgered, "Geodesy by radio interferometry: Effects of atmospheric modeling errors on estimates of baseline length," *Radio Sci.*, vol. 20, no. 6, pp. 1593–1607, Nov. 1985.

[38] R. Jolivet et al., "Improving InSAR geodesy using global atmospheric models," *J. Geophys. Research: Solid Earth*, vol. 119, no. 3, pp. 2324–2341, Mar. 2014.

[39] M.-P. Doin, C. Lasserre, G. Peltzer, O. Cavalié, and C. Doubre, "Corrections of stratified tropospheric delays in SAR interferometry: Validation with global atmospheric models," *J. Appl. Geophysics*, vol. 69, no. 1, pp. 35–50, Sep. 2009.

[40] H. Tarayre and D. Massonnet, "Effects of a refractive atmosphere on interferometric processing," in *Proc. IEEE Int. Geosci. Remote Sens. Symp.*, vol. 2, Aug. 1994, pp. 717–719.

[41] A. Rucci, A. Ferretti, A. Monti Guarnieri, and F. Rocca, "Sentinel 1 SAR interferometry applications: The outlook for sub millimeter measurements," *Remote Sens. Environ.*, vol. 120, pp. 156–163, May 2012.

[42] A. Recchia, A. M. Guarnieri, A. Broquetas, and J. Ruiz-Rodon, "Assesment of atmospheric phase screen impact on geosynchronous SAR," in *Proc. IEEE Geosci. Remote Sens. Symp.*, Jul. 2014, pp. 2253–2256.

[43] A. N. Kolmogorov, "The local structure of turbulence in incompressible viscous fluid for very large Reynolds numbers," *Proc. Roy. Soc. London. Ser. A, Math. Phys. Sci.*, vol. 434, no. 1890, pp. 9–13, Jul. 1991.

[44] M. Lagasio et al., "A synergistic use of a high-resolution numerical weather prediction model and high-resolution Earth observation products to improve precipitation forecast," *Remote Sens.*, vol. 11, no. 20, p. 2387, Oct. 2019.

[45] X. Dong, J. Hu, C. Hu, T. Long, Y. Li, and Y. Tian, "Modeling and quantitative analysis of tropospheric impact on inclined geosynchronous SAR imaging," *Remote Sens.*, vol. 11, no. 7, p. 803, Apr. 2019.

[46] X. Song, G. Venuti, A. V. Monti-Guarnieri, and M. Manzoni, "Augmented iterative tropospheric decomposition strategy for GNSS-based zenith tropospheric delay map generation," *Environ. Model. Softw.*, vol. 194, Oct. 2025, Art. no. 106669.

[47] J. R. Rodon, A. Broquetas, A. M. Guarnieri, and F. Rocca, "Geosynchronous SAR focusing with atmospheric phase screen retrieval and compensation," *IEEE Trans. Geosci. Remote Sens.*, vol. 51, no. 8, pp. 4397–4404, Aug. 2013.

[48] E. Pichelli et al., "InSAR water vapor data assimilation into mesoscale model MM5: Technique and pilot study," *IEEE J. Sel. Topics Appl. Earth Observ. Remote Sens.*, vol. 8, no. 8, pp. 3859–3875, Aug. 2015.

[49] F. Meyer, R. Bamler, N. Jakowski, and T. Fritz, "The potential of low-frequency SAR systems for mapping ionospheric TEC distributions," *IEEE Geosci. Remote Sens. Lett.*, vol. 3, no. 4, pp. 560–564, Oct. 2006.

[50] B. Zolesi and L. R. Cander, "Ionospheric models for prediction and forecasting," in *Ionospheric Prediction and Forecasting*. Berlin, Germany: Springer, 2014, pp. 101–121.

[51] W. Guo, P. Xiao, and X. Gao, "Compensation of background ionospheric effect on L-band geosynchronous SAR with fully polarimetric data," *Remote Sens.*, vol. 15, no. 15, p. 3746, Jul. 2023.

[52] C. Cesaroni, C. Marcocci, E. Pica, and L. Spogli, "Electronic space weather upper atmosphere database (ESWUA)-total electron content (TEC) data," Tech. Rep., 2020.

[53] J. C. Curlander and R. N. McDonough, *Synthetic Aperture Radar*, vol. 11. Hoboken, NJ, USA: Wiley, 1991.

[54] D. L. Hysell and E. B. Shume, "Electrostatic plasma turbulence in the topside equatorial f region ionosphere," *J. Geophys. Research: Space Phys.*, vol. 107, no. A10, pp. 1–12, Oct. 2002.

[55] L. Iannini and A. Monti Guarnieri, "Atmospheric phase screen in ground-based radar: Statistics and compensation," *IEEE Geosci. Remote Sens. Lett.*, vol. 8, no. 3, pp. 537–541, May 2011.

[56] F. Onn, *Modeling Water Vapor Using GPS with Application to Mitigating In SAR Atmospheric Distortions*, vol. 67. Stanford, CA, USA: Stanford University (Department of Electrical Engineering), 2006.

[57] *Estimation of Local-Scale Precipitable Water Vapor Distribution Around Each GNSS Station Using Slant Path Delay: Evaluation of a Severe Tornado Case Using High-Resolution NHM*, Japan Sci. Technol. Agency (JST), Tokyo, Japan, 2015.

[58] B. M. Welsh, "Fourier-series-based atmospheric phase screen generator for simulating anisoplanatic geometries and temporal evolution," *Proc. SPIE*, vol. 3125, pp. 327–338, May 2025.

[59] W. Sheng and S. E. Hobbs, "Research on compensation of motion, Earth curvature and tropospheric delay in GEOSAR," *Acta Astronautica*, vol. 68, nos. 11–12, pp. 2005–2011, Jun. 2011.

[60] H.-S. Jung, D.-T. Lee, Z. Lu, and J.-S. Won, "Ionospheric correction of SAR interferograms by multiple-aperture interferometry," *IEEE Trans. Geosci. Remote Sens.*, vol. 51, no. 5, pp. 3191–3199, May 2013.

[61] S. Schön and G. Kermarrec, "Turbulence theory," in *Handbook of Geomathematics*, W. Freeden, M. Z. Nashed, and T. Sonar, Eds., Heidelberg, Germany: Springer, 2015, pp. 1297–1348.

[62] A. A. Stotskii, "Path length fluctuations through the Earth troposphere: Turbulent model and data of observations," *Refraction Transatmospheric Signals Geodesy*, no. 36, pp. 179–182, May 1992.

[63] L. C. Andrews, R. L. Phillips, and A. R. Weeks, "Propagation of a Gaussian-beam wave through a random phase screen," *Waves Random Media*, vol. 7, no. 2, pp. 229–244, Apr. 1997.

[64] E. Realini, T. Tsuda, K. Sato, M. Oigawa, and Y. Iwaki, "Analysis of the temporal and spatial variability of the wet troposphere at a local scale by high-rate PPP using a dense GNSS network," in *Proc. 25th Int.Tech. Meeting Satellite Division Institute Navigation*, vol. 5, Sep. 2012, pp. 1–18.

[65] J. G. Powers et al., "The weather research and forecasting model: Overview, system efforts, and future directions," *Bull. Amer. Meteorological Soc.*, vol. 98, no. 8, pp. 1717–1737, Aug. 2017.

[66] S.-Y. Hong, Y. Noh, and J. Dudhia, "A new vertical diffusion package with an explicit treatment of entrainment processes," *Monthly Weather Rev.*, vol. 134, no. 9, pp. 2318–2341, Sep. 2006.

[67] M. J. Iacono, J. S. Delamere, E. J. Mlawer, M. W. Shephard, S. A. Clough, and W. D. Collins, "Radiative forcing by long-lived greenhouse gases: Calculations with the AER radiative transfer models," *J. Geophys. Res., Atmos.*, vol. 113, no. D13, pp. 1–16, Jul. 2008.

[68] E. J. Mlawer, S. J. Taubman, P. D. Brown, M. J. Iacono, and S. A. Clough, "Radiative transfer for inhomogeneous atmospheres: RRTM, a validated correlated-K model for the longwave," *J. Geophys. Res., Atmos.*, vol. 102, no. D14, pp. 16663–16682, Jul. 1997.

[69] M. J. Iacono, E. J. Mlawer, S. A. Clough, and J.-J. Morcrette, "Impact of an improved longwave radiation model, RRTM, on the energy budget and thermodynamic properties of the NCAR community climate model, CCM3," *J. Geophys. Res., Atmos.*, vol. 105, no. D11, pp. 14873–14890, Jun. 2000.

[70] T. G. Smirnova, J. M. Brown, and S. G. Benjamin, "Performance of different soil model configurations in simulating ground surface temperature and surface fluxes," *Monthly Weather Rev.*, vol. 125, no. 8, pp. 1870–1884, Aug. 1997.

[71] T. G. Smirnova, J. M. Brown, S. G. Benjamin, and D. Kim, "Parameterization of cold-season processes in the MAPS land-surface scheme," *J. Geophys. Res., Atmos.*, vol. 105, no. D3, pp. 4077–4086, Feb. 2000.

[72] J. Han and H.-L. Pan, "Revision of convection and vertical diffusion schemes in the NCEP global forecast system," *Weather Forecasting*, no. 26, Mar. 2011, Art. no. 110324113650092.

[73] L. Apicella et al., "The predictive capacity of the high resolution weather research and forecasting model: A year-long verification over Italy," *Bull. Atmos. Sci. Technol.*, vol. 2, nos. 1–4, p. 3, Dec. 2021.

[74] B. Zolesi and L. R. Cander, *Ionospheric Spatial and Temporal Variations*. Berlin, Germany: Springer, 2014, pp. 81–99.

[75] NOAA Space Weather Prediction Center. *Solar Cycle Progression*. Accessed: Oct. 29, 2025. [Online]. Available: https://www.swpc.noaa.gov/products/solar-cycle-progression

[76] *Sunspot Number: International Sunspot Number Monthly Data, 2000–2025*, Royal Observatory of Belgium, Brussels, Belgium, 2000.

[77] F. J. Meyer, "Performance requirements for ionospheric correction of low-frequency SAR data," *IEEE Trans. Geosci. Remote Sens.*, vol. 49, no. 10, pp. 3694–3702, Oct. 2011.